

# Nanoarray Structures for Artificial Photosynthesis

Liangqiu Tian, Qi Xin, Chang Zhao, Guancai Xie, Muhammad Zain Akram, Wenrong Wang, Renping Ma, Xinrui Jia, Beidou Guo,\* and Jian Ru Gong\*

Conversion and storage of solar energy into fuels and chemicals by artificial photosynthesis has been considered as one of the promising methods to address the global energy crisis. However, it is still far from the practical applications on a large scale. Nanoarray structures that combine the advantages of nanosize and array alignment have demonstrated great potential to improve solar energy conversion efficiency, stability, and selectivity. This article provides a comprehensive review on the utilization of nanoarray structures in artificial photosynthesis of renewable fuels and high value-added chemicals. First, basic principles of solar energy conversion and superiorities of using nanoarray structures in this field are described. Recent research progress on nanoarray structures in both abiotic and abiotic–biotic hybrid systems is then outlined, highlighting contributions to light absorption, charge transport and transfer, and catalytic reactions (including kinetics and selectivity). Finally, conclusions and outlooks on future research directions of nanoarray structures for artificial photosynthesis are presented.

## 1. Introduction

Energy crisis is one of the most important issues impacting the global politics, economy, security, and environment. Taking into account the rapid depletion of traditional energy resources and the ever increasing environmental pollution, it is the need of the hour to introduce alternative energy sources.<sup>[1–5]</sup> Solar energy is an abundant and clean energy resource obtained on the planet. Each year, ≈100 000 TW of solar energy reaches our planet, of which ≈36 000 TW arrives on land.<sup>[6]</sup> However, two requirements must be met for sustainable development of solar energy. First, the means of solar energy conversion, storage, and distribution should be environmentally friendly, in order to protect the ecosystem. Second,

a stable and constant energy flux must be guaranteed. Due to the daily and seasonal changes in sunlight, solar energy needs to be effectively converted into chemical fuels, which could then be stored, transported, and used on demand.<sup>[7]</sup> In this scenario, the cost-effective sustainable conversion of solar energy into fuels as well as high value-added chemicals by artificial photosynthesis,<sup>[8]</sup> which can mimic the function of chloroplasts in natural photosynthesis,<sup>[9]</sup> is regarded as one of the Holy Grails of the 21st century science.<sup>[2,10–14]</sup> In artificial photosynthesis, water splitting and carbon dioxide (CO<sub>2</sub>) reduction reaction (CO<sub>2</sub>RR) are the two most important reactions, wherein the subsequent combustion of produced solar fuels does not lead to additional CO<sub>2</sub> emissions because of the closed carbon cycle (Figure 1a).

In addition, N<sub>2</sub> reduction reaction (NRR) is another vital reaction that provides top value-added chemicals such as ammonia (NH<sub>3</sub>) without emitting the CO<sub>2</sub> biproduct.<sup>[15,16]</sup>

### 1.1. The Principle of Artificial Photosynthesis

Semiconductors are the most commonly used materials for artificial photosynthesis. The eligibility of a semiconducting material to drive a particular reaction of artificial photosynthesis is governed by its bandgap and band edge positions with respect to the reaction of interest.<sup>[18–20]</sup> From the point of view of Gibbs free energy change under the standard conditions of 1 atm pressure and 298 K ( $\Delta G^0$ ), the splitting of water into H<sub>2</sub> and O<sub>2</sub> (Equation (1)), the reduction of CO<sub>2</sub> to hydrocarbons (Equations (2)–(5)), and the fixation of N<sub>2</sub> to NH<sub>3</sub> (Equation (6)) are all energetically unfavorable (uphill) reactions (Figure 1b), and their corresponding  $\Delta G^0$  values are positive (e.g.,  $\Delta G^0$  of water splitting and reduction of CO<sub>2</sub> to CH<sub>4</sub> are 237 and 818 kJ mol<sup>-1</sup>, respectively). However, following the photoexcitation of the reactant, these reactions become energetically favorable ( $\Delta G^0 < 0$ ).<sup>[12,21–23]</sup> The potential difference of electrochemical reactions under the standard conditions of 1 atm pressure and 298 K ( $\Delta E^0$ ) can be calculated using the relation  $\Delta E^0 = \Delta G^0/nF$ , where  $n$  is the number of electrons exchanged and  $F$  is the Faraday constant.<sup>[12]</sup> Since the hydrogen evolution reaction (HER) in water splitting can proceed through a two-electron pathway, the  $\Delta E^0$  to drive this reaction is 1.23 V, which means that the theoretical minimum bandgap for water splitting is 1.23 eV;

L. Tian, Dr. Q. Xin, C. Zhao, Dr. G. Xie, Dr. M. Z. Akram, Dr. W. Wang, Dr. R. Ma, X. Jia, Dr. B. Guo, Prof. J. R. Gong  
Chinese Academy of Sciences (CAS) Center for Excellence in Nanoscience

CAS Key Laboratory for Nanosystem and Hierarchical Fabrication  
National Center for Nanoscience and Technology  
Beijing 100190, P. R. China

E-mail: guobd@nanoctr.cn; gongjr@nanoctr.cn

L. Tian, C. Zhao, Dr. G. Xie, Dr. M. Z. Akram, X. Jia, Dr. B. Guo, Prof. J. R. Gong  
School of Chemical Sciences  
University of CAS  
Beijing 100049, P. R. China

The ORCID identification number(s) for the author(s) of this article can be found under <https://doi.org/10.1002/smll.202006530>.

DOI: 10.1002/smll.202006530

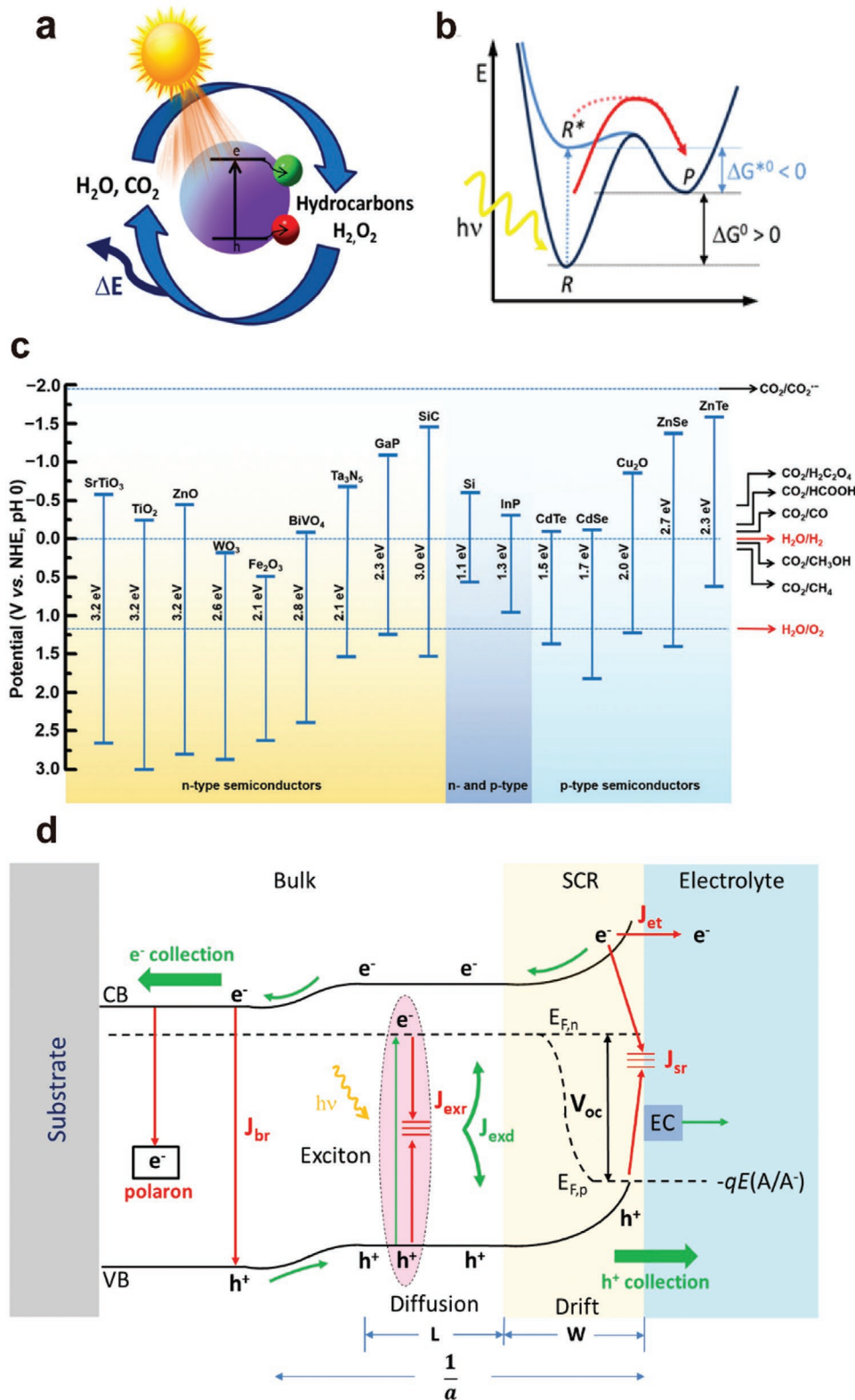
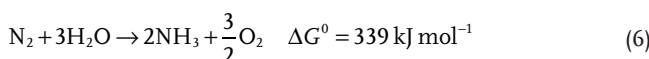
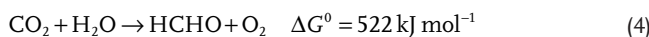
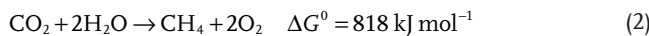
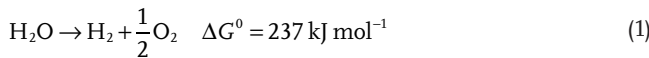


**Figure 1.** a) Closed cycle of solar energy storage by conversion of  $H_2O$  and  $CO_2$  into chemical fuels. The stored energy can be released on demand through a reverse reaction. b) Energy diagrams of photoactivated endergonic reactions. Following the photoexcitation of reactant  $R$ , the reaction becomes energetically favorable ( $\Delta G^{*0} < 0$ ), represented by the dotted red arrow. Reproduced with permission.<sup>[12]</sup> Copyright 2018, American Chemical Society. c) Conduction band (top bar) and valence band (bottom bar) positions of some representative semiconductors and the corresponding redox potentials of water splitting and  $CO_2$  reduction versus NHE at pH 0. Reproduced with permission.<sup>[17]</sup> Copyright 2018, Royal Society of Chemistry.

while for the reduction of CO<sub>2</sub> to CH<sub>4</sub>, which is an eight-electron reaction, the lowest theoretical bandgap requirement is 1.06 eV<sup>[6,12,20,21,24]</sup>



Taking the water splitting as an example, we need to consider the thermodynamic losses (0.3–0.4 eV) for charge carrier transport and the overpotential requirement for adequate surface reaction kinetics (0.4–0.6 eV), so a minimum bandgap of ≈1.8 eV is required, corresponding to light absorption at ≈700 nm. The maximum value of the bandgap is determined by the solar spectrum, and the rapid drop in sunlight intensity below 390 nm imposes an upper limit of 3.2 eV on the bandgap. This means the optimum bandgap value of a single semiconductor to carry out water splitting practically lies in the range of 1.8–3.2 eV.<sup>[6,19]</sup>

In addition to a suitable bandgap energy, an ideal band edge position is also optimal for single semiconducting materials for effective artificial photosynthesis.<sup>[6,17]</sup> Considering thermodynamic band positions, the conduction band minimum (CBM) of the photocathode should be more negative than the reduction potential of H<sub>2</sub>O (0 V vs normal hydrogen electrode (V<sub>NHE</sub>) at pH 0) or of CO<sub>2</sub> (varying depending on products), while the valence band maximum (VBM) of the photoanode should be more positive than the oxidation potential of H<sub>2</sub>O (+1.23 V<sub>NHE</sub> at pH 0).<sup>[12,17,20,25,26]</sup> Band structures of some widely used semiconductors for solar energy conversion with respect to the redox potentials for water splitting and CO<sub>2</sub>RR are shown in Figure 1c.<sup>[17]</sup> These representative semiconductor materials have sufficient bandgap energies as well as suitable band edge positions to drive solar energy conversion effectively: the n-type semiconductors can be used as photoanodes for oxygen evolution reaction (OER); the p-type semiconductors can be used as photocathodes for CO<sub>2</sub>RR; Si and InP can be doped to either n-type or p-type semiconductors for the corresponding reactions.

Three key physiochemical processes of semiconductors are involved in artificial photosynthesis (Figure 1d; a photoelectrochemical (PEC) semiconductor model system), which contribute

positively to the system efficiency.<sup>[27,28]</sup> The first process involves the light absorption under sun irradiation, resulting in generation of excitons (electron–hole pairs bound by Coulomb interaction) in the semiconductor;<sup>[12]</sup> these excitons rapidly dissociate in inorganic bulk semiconductors because their binding energies ( $\approx 0.01$  eV)<sup>[29–31]</sup> are lower than the thermal energy ( $\approx 0.025$  eV) at room temperature.<sup>[32]</sup> In contrast, conjugated polymers, organic small molecules, and low-dimensional inorganic nanostructures with quantum size effects, where the electron–hole pairs are confined to a space smaller than the Bohr exciton radius, have relatively high exciton binding energies (typically ranging from 0.25 to 1.2 eV) due to their weak intermolecular electronic coupling and low dielectric constants,<sup>[30,33–35]</sup> meaning additional energy is needed to dissociate photogenerated excitons for free charge carriers. The second process is the transport and transfer of free charge carriers to the semiconductor surface.<sup>[6]</sup> Band bending of the space charge region (SCR) with a width of W at the semiconductor/electrolyte interface is the driving force for the separation of photogenerated electrons and holes.<sup>[36]</sup> Only the charge carriers generated within the carrier collection distance, i.e., the sum of the carrier diffusion length ( $L$ ) and SCR width ( $W$ ), can reach the semiconductor surface.<sup>[37]</sup> In the third process, the redox reactions occur at the semiconductor/electrolyte interface.<sup>[6]</sup> Usually, abiotic or biotic electrocatalysts (ECs) are loaded on the surface of semiconductors, which can promote the charge separation and transfer driven by the interface/junction formed between semiconductors and ECs, accelerate the catalytic kinetics by lowering the activation energy, and also improve the catalytic selectivity. However, the unwanted charge recombination during these processes such as bulk recombination, SCR recombination, surface recombination due to defects, tunneling current, and electron-transfer current associated with majority carriers traversing the interfacial barrier are detrimental to the system efficiency.<sup>[7]</sup> Therefore, understanding and controlling the relevant kinetic processes is essential in the design of efficient artificial photosynthetic systems.

## 1.2. Performance Evaluation Parameters of Artificial Photosynthesis

The standard evaluation parameters of performance are needed in artificial photosynthesis, which can provide rational comparisons of different systems. For PEC systems, the common performance evaluation parameters include i) solar-to-fuel conversion efficiency (STF; Equation (7)), ii) the applied bias photon-to-current efficiency (ABPE; Equation (9)), and iii) incident photon-to-current efficiency (IPCE; Equation (10)).<sup>[6,38,39]</sup>

STF conversion efficiency is considered as the benchmark value to compare different photoelectrodes in different electrolytes, which describes the overall efficiency of a PEC device exposed to the broadband solar air mass 1.5 global (AM 1.5G)

d) Schematic illustration of charge transfer pathways in an n-type semiconductor-based PEC model device under solar irradiation at zero bias. CB, conduction band; E<sub>F</sub>, Fermi energy level; VB, valence band; exr, exciton recombination; exd, exciton dissociation; br, bulk recombination; sr, surface recombination; et, electron transfer; EC, electrocatalyst; SCR, space charge region; hole collection distance = hole diffusion length ( $L$ ) + SCR width ( $W$ ); the light penetration depth  $\alpha^{-1}$  (the reciprocal of light absorption coefficient) refers to the distance after which the light intensity is reduced to  $1/e$  of the original value.

illumination under zero bias conditions. Generally, the STF efficiency is measured in a two-electrode system with direct short-circuiting of the working electrode (WE) and the counter electrode (CE). Apart from the direct measurement of the product yield by gas chromatography to calculate the chemical energy produced, there is an alternative and simpler method to calculate  $\eta_{\text{STF}}$

$$\eta_{\text{STF}} = \frac{J_{\text{sc}} (\text{mA cm}^{-2}) \times \Delta E^0 (\text{V}) \times \eta_{\text{F}}}{P_{\text{light}} (\text{mW cm}^{-2})} \times 100\% \quad (7)$$

where  $J_{\text{sc}}$  is current density at short circuit;  $\Delta E^0$  is the thermodynamics energy stored in the PEC reactor (e.g.,  $\Delta E^0$  of water splitting is 1.23 V);  $P_{\text{light}}$  is 100 mW cm<sup>-2</sup> (AM 1.5G) and  $\eta_{\text{F}}$  is the Faradaic efficiency, which can be calculated by Equation (8)

$$\eta_{\text{F}} = \frac{e_{\text{output}}}{e_{\text{input}}} \times 100\% = \frac{n (\text{mol}) \times y}{Q (\text{Coulomb})} \times 100\% \quad (8)$$

where  $n$  is the moles of product;  $y$  is the number of electrons needed for the reaction;  $Q$  is the calculated electric charge and  $F$  is the Faraday constant (96 485 C mol<sup>-1</sup>).

However, due to insufficient photovoltage, an external bias between the WE and CE is generally required to ensure the PEC reactions. Therefore, ABPE and IPCE are used more frequently for the evaluation of the solar conversion efficiency in actual PEC devices

$$\text{ABPE} = \frac{J_{\text{Ph}} (\text{mA cm}^{-2}) \times (\Delta E^0 (\text{V}) - V_{\text{app}} (\text{V})) \times \eta_{\text{F}}}{P_{\text{light}} (\text{mW cm}^{-2})} \quad (9)$$

where  $J_{\text{Ph}}$  is the photocurrent density at  $V_{\text{app}}$ ;  $V_{\text{app}}$  is the applied voltage between the WE and CE;  $\Delta E^0$  is the thermodynamics energy stored in the PEC reactor;  $P_{\text{light}}$  is the power density of the incident light;  $\eta_{\text{F}}$  is the Faradaic efficiency

$$\text{IPCE} = \frac{h \times c}{e} \times \frac{J_{\text{Ph}}}{P_{\text{mono}} \times \lambda} = \frac{1239.8 (\text{V} \times \text{nm}) \times J_{\text{Ph}} (\text{mA cm}^{-2})}{P_{\text{mono}} (\text{mW cm}^{-2}) \times \lambda (\text{nm})} \times 100\% \quad (10)$$

where  $h$  is Planck's constant;  $c$  is the speed of light;  $e$  is the charge of electrons;  $J_{\text{Ph}}$  is the photocurrent density;  $\lambda$  is the wavelength of monochromatic light and  $P_{\text{mono}}$  is the power density of the monochromatic light at  $\lambda$ .

In addition, selectivity and stability are also important, especially the selectivity of CO<sub>2</sub>RR to the target product (Equation (11))<sup>[39]</sup>

$$\text{Product selectivity} = \frac{\text{Amount of electrons required for the target product}}{\text{Total amount of electrons consumed for CO}_2 \text{ reduction}} \quad (11)$$

### 1.3. Advantages of Nanoarray Structures in Artificial Photosynthesis

So far, materials with a wide variety of morphologies have been fabricated for solar energy conversion to optimize their

performance. As a common and easily synthesized type, thin-film structures are considered suitable for enhanced charge transport and reduced material cost as compared to their bulk counterparts, and have been therefore, used in artificial photosynthesis.<sup>[19,40]</sup> However, their reduced thickness may go far lower than the light penetration depth  $\alpha^{-1}$ , leading to decreased light absorption as well as relatively low solar energy conversion efficiencies. Therefore, a much sought-after aim is to increase light absorption without compromising on charge transport so as to maximize the solar energy conversion efficiencies. Using nanostructures is an alternative strategy to achieve high performance since they can overcome the drawbacks of thin films mentioned above owing to their unique nanosize morphologies.<sup>[5,36,41,42]</sup> So far, many reports have demonstrated the outstanding solar energy conversion performance of semiconductors with nanostructures compared to those without nanostructures.<sup>[26,43–46]</sup>

In particular, nanoarray structures, which are large-scale alignment of oriented nanostructure units on the substrate or an arrangement of elements of closely related and systematically varied nanostructures,<sup>[47,48]</sup> hold great potential in artificial photosynthesis in view of the following key features: 1) array structures can harvest extra light by various strategies such as multiple light scattering and antireflection among the nanostructure units, thereby achieving enhanced light absorption;<sup>[47,49,50]</sup> 2) nanostructures can shorten the carrier collection distance and increase the proportion of SCR to the bulk for promoting charge separation;<sup>[27,36,51–53]</sup> 3) nanoarray structures have a higher specific surface area than planar film structures, supplying more chemisorption sites and active sites for catalytic reactions, providing more sites for loading the abiotic or biotic ECs, offering easier access to electrolytes and reactants, and thus accelerating the catalytic kinetics and improving the catalytic selectivity.<sup>[47,54–56]</sup> Additionally, the nanoarray can withstand more strain than the planar film structure, especially when being in contact with a lattice-mismatched substrate.<sup>[57]</sup> In view of these advantages, nanoarray structures are deemed ideal to improve the efficiencies of the aforementioned important processes in artificial photosynthesis. The common synthesis methods of nanoarray structures are vapor–liquid–solid growth, solid–liquid–solid growth, hydro/solvothermal growth, chemical bath deposition growth, template-based growth, and electrochemical growth.<sup>[38,47]</sup> Not surprisingly, many examples, such as 1D nanowire,<sup>[15,58,59]</sup> nanorod<sup>[60–62]</sup> and nanotube arrays (NTAs),<sup>[63–65]</sup> 2D nanoflakes<sup>[66–68]</sup> and nanosheet arrays,<sup>[69–71]</sup> and 3D inverse opals (IOs),<sup>[72–74]</sup> solid and hollow nanospheres (NSs),<sup>[75,76]</sup> as well as branched nanoarray structures,<sup>[77–80]</sup> have demonstrated the effectiveness of nanoarray structures in solar energy conversion and storage for fuels and chemicals. For one special type of materials/structures of nanoarrays or some specific process involved in artificial photosynthesis, please refer to the recent review papers such as heterogeneous nanostructure array for electrochemical energy conversion,<sup>[47]</sup> light management with patterned nanostructure arrays for photocatalysis,<sup>[49]</sup> hierarchical architectures to trap light for efficient PEC cells,<sup>[81]</sup> nanoarrays with rapid charge transport for PEC applications,<sup>[82]</sup> branched titania nanostructures for efficient energy conversion,<sup>[83]</sup> FeO-based nanostructures and nanohybrids

for PEC water splitting,<sup>[84]</sup> and metal oxide nanoarray-based photoanodes for PEC water splitting.<sup>[38]</sup>

Although there have been a few review articles discussing the nanoarrays applied for artificial photosynthesis, most of them are not comprehensive enough to summarize the material types or functions. To fulfill this gap, in this review, the recent research progress in the development of various nanoarray structures in both abiotic and abiotic–biotic hybrid artificial photosynthetic systems is reviewed in detail, highlighting their contributions to light absorption, charge transport and transfer, and catalytic reactions (including kinetics and selectivity), which are key factors involved in solar energy conversion. First, a number of nanoarray structures with increased intensity and/or extended spectral range for light absorption enhancement are discussed. Second, both single- and dual-bandgap nanoarray structures are presented to show different charge transport and transfer pathways and mechanisms to promote charge separation and reduce charge recombination. Third, nanoarray structures for improving catalytic kinetics as well as selectivity are also reviewed in both abiotic and enzyme-involved abiotic–biotic hybrid systems for artificial photosynthesis. Finally, conclusions and outlooks about nanoarray structures in artificial photosynthesis are outlined.

## 2. Light Absorption

Light absorption is the first key process in solar energy conversion, wherein the incident photons convert into electron–hole pairs for the redox reactions.<sup>[85,86]</sup> Till date, several attempts have been made to enhance light absorption in various nanoarray structures, and among them the one with the most optimum results are summarized in **Figure 2**. The introduction of multiple light scattering,<sup>[87–90]</sup> antireflection,<sup>[91–94]</sup> slow light effect,<sup>[95,96]</sup> surface plasmon resonance (SPR),<sup>[97–99]</sup> bandgap narrowing,<sup>[69,100]</sup> and photosensitization,<sup>[101–103]</sup> can increase the light absorption intensity as well as extend the spectral range of the nanoarray structures. Furthermore, the hybrid structures combining more than one light management strategies have successfully achieved synergistic effects in light absorption. The specific strategies will be detailed in the subsections below, respectively.

### 2.1. Multiple Light Scattering

When the size of the units in the nanoarray is larger than the wavelength of incident light, light scattering effect, which comes from the interactions between the periodically aligned

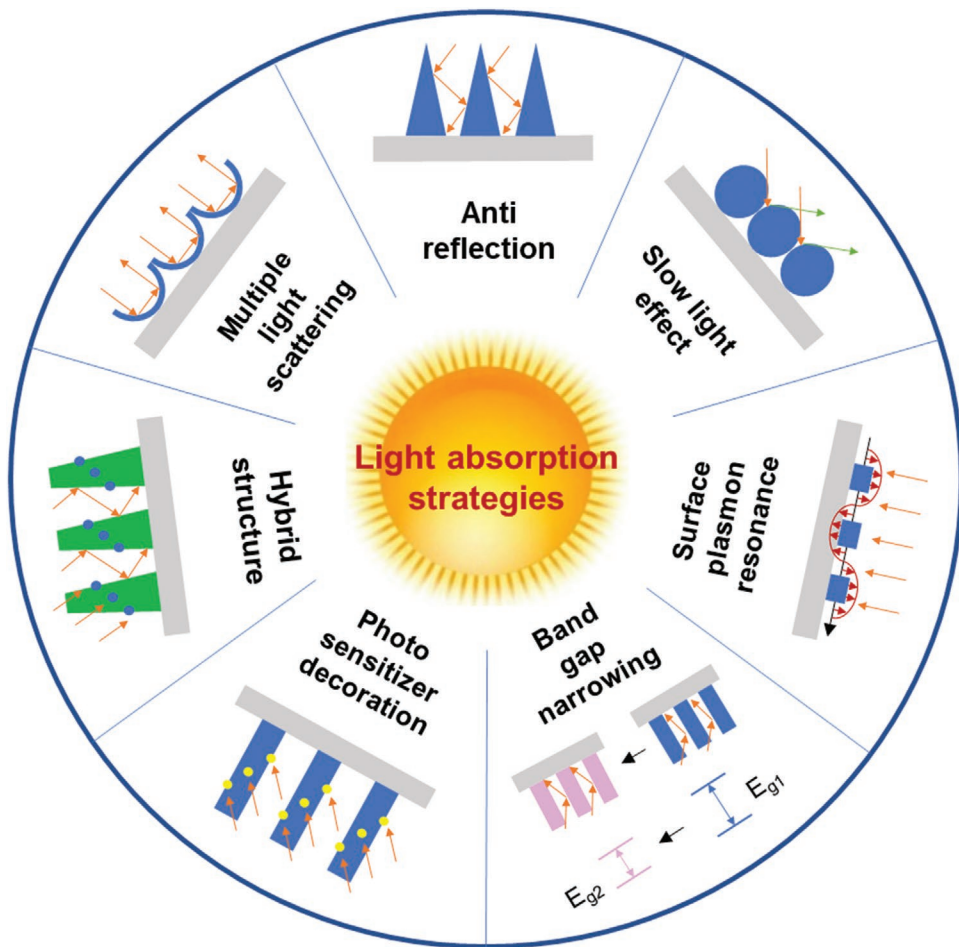


**Figure 2.** Schematic diagram of common strategies for light absorption enhancement based on nanoarray structures in artificial photosynthesis.

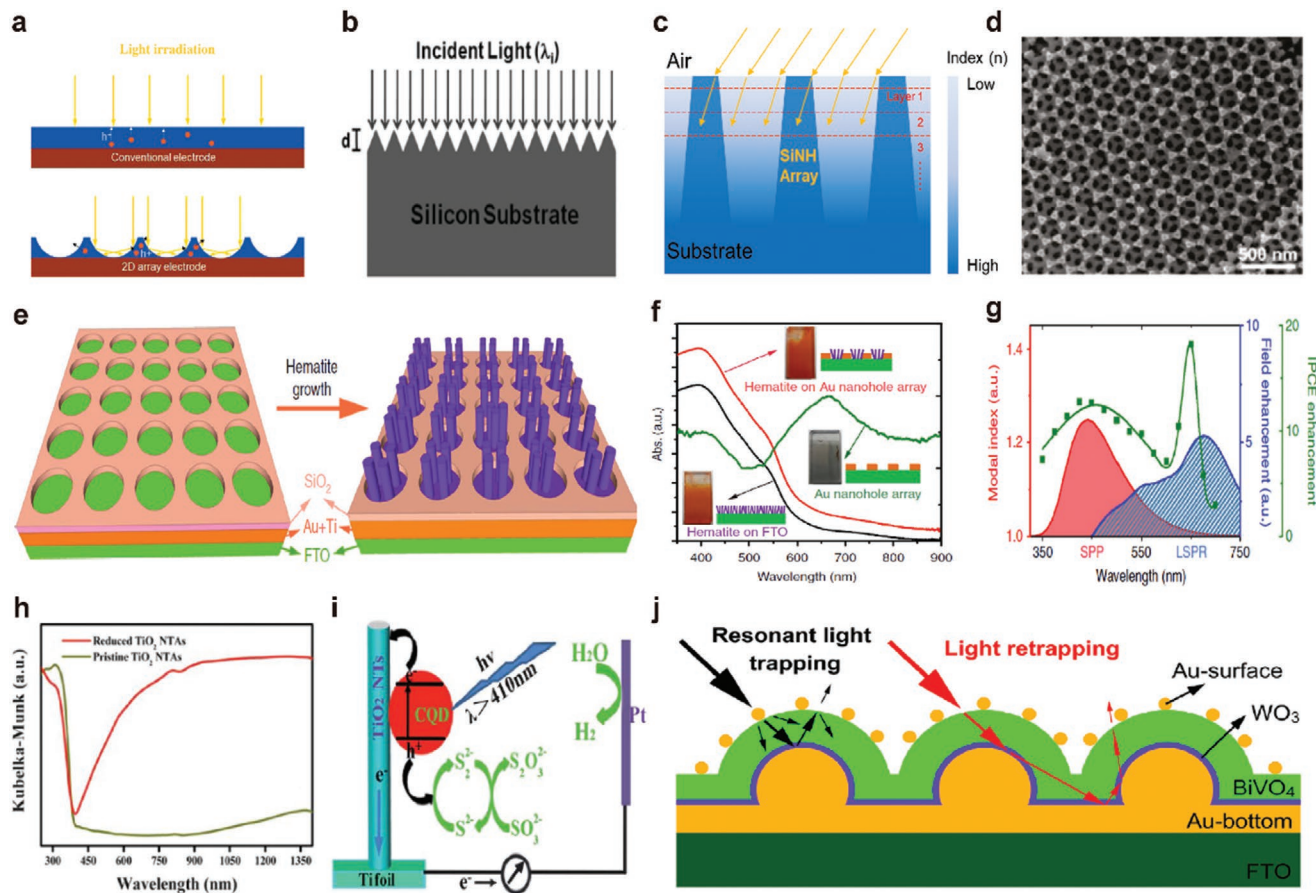


**Figure 3.** a) Schematic showing the light scattering mechanism of the conversion efficiency enhancement within the  $\text{Bi}_2\text{WO}_6$  nanovoid array photoanode compared to the conventional  $\text{Bi}_2\text{WO}_6$  thin film. Reproduced with permission.<sup>[88]</sup> Copyright 2013, Wiley-VCH GmbH. b) Schematic presentation of SWS. Reproduced with permission.<sup>[104]</sup> Copyright 2010, Elsevier B.V. c) Gradient refraction optical path in the tapered SiNH array photocathode. d) SEM image of  $\text{WO}_3$  inverse opals (IOs). Reproduced with permission.<sup>[96]</sup> Copyright 2011, American Chemical Society. e) Scheme for the growth of the hematite nanorod array on the Au nanohole array. f) UV-visible absorption spectra for 150 nm long hematite nanorods on the bare FTO (black line) and on the Au nanohole array pattern (red line), as well as an individual Au nanohole array (green line). g) The waveguiding efficiency and local plasmonic field enhancement are illustrated to precisely reveal the trend in IPCE. Reproduced with permission.<sup>[105]</sup> Copyright 2013, Springer Nature. h) UV-visible–NIR diffuse reflectance spectra of pristine and reduced  $\text{TiO}_2$  NTAs. Reproduced with permission.<sup>[106]</sup> Copyright 2013, Royal Society of Chemistry. i) The schematic diagram of the sensitization mechanism of the CQDs deposited on the surface  $\text{TiO}_2$  NTs. Reproduced with permission.<sup>[107]</sup> Copyright 2013, Royal Society of Chemistry. j) Schematic illustration of the design rationales for resonant light trapping and light retrapping in the antenna/spacer/reflector-based Au-surface/ $\text{BiVO}_4$ / $\text{WO}_3$ /Au-bottom nanopatterned photoanode. Reproduced with permission.<sup>[108]</sup> Copyright 2018, Elsevier B.V.

nanoarray and the exposed light, can result in an increased optical path length; thereafter, it enhances light absorption by trapping the light inside the nanoarray.<sup>[49,109]</sup>

The nanoarray structures with the light scattering effect in solar energy conversion can be roughly divided into two categories:<sup>[49]</sup> one is the conductive nanoarray substrates such as fluorine-doped tin oxide (FTO), aluminum-doped zinc oxide (AZO), and metal Ti<sup>[110–112]</sup> coated with light absorbing materials, and the other is the semiconductor nanostructures such as nanovoid arrays, nanowire arrays, nanotube arrays, urchin-like structure arrays, and nanorod@nanobowl structure arrays.<sup>[88,113–116]</sup> For the former, one example is the patterned FTO (p-FTO) coated with  $\alpha\text{-Fe}_2\text{O}_3$ , fabricated via a reactive ion etching method.<sup>[110]</sup> Owing to the light scattering effect of the 3D p-FTO nanoarray, which interacts well with the exposing light,  $\alpha\text{-Fe}_2\text{O}_3$ /p-FTO demonstrates increased light absorption as well as photocurrent ( $1.88 \text{ mA cm}^{-2}$  at

$1.5 \text{ V}_{\text{RHE}}$ ), compared to  $\alpha\text{-Fe}_2\text{O}_3$ /bare FTO (photocurrent:  $1.1 \text{ mA cm}^{-2}$  at  $1.5 \text{ V}_{\text{RHE}}$ ) for PEC water splitting. For the latter, a self-assembled  $\text{Bi}_2\text{WO}_6$  nanovoid array photoanode shows the increased intensity of absorbed light owing to multiple light scattering and thus elongated optical path among the nanovoid units (Figure 3a), compared to the corresponding planar sample.<sup>[88]</sup> As a result, the photocurrent density of the  $\text{Bi}_2\text{WO}_6$  nanovoid array is 2–4 times higher than the planar one over the entire potential range from  $-0.3$  to  $0.4 \text{ V}$  versus Ag/AgCl. Therefore, it can be concluded that the nanoarray structures with the effect of multiple light scattering are able to increase the light absorption. However, the multiple light scattering effect can only achieve limited increase in light absorption intensity by elongation of the optical path length. Therefore, new ways such as extension of the spectral range, are also needed to further promote the light absorption ability of the nanoarrays.

## 2.2. Antireflection

Light absorption can also be enhanced by reducing light loss occurring from reflection off the front surface of artificial photosynthetic systems.<sup>[91,117–119]</sup> Some particular nanoarray structures, i.e., nanorod, nanocone, and nanopillar arrays, have displayed high light absorption capacities owing to effective antireflection of light.<sup>[49]</sup>

A subwavelength structure (SWS; Figure 3b,c), which is a surface-relief grating with a period smaller than the incident light wavelength, behaves as an antireflective surface.<sup>[104,120]</sup> As shown in SWS (Figure 3c), the interface area between air and the substrate can be divided into a large number of layers; each layer has an effective index, which can be deduced with the weighted average of the refractive indexes of air and the substrate, according to their respective area ratio. As a result, the effective refractive index gradually changes from the low number (air on the top) to the high number (substrate at the bottom). In this way, the strong reflection caused by the sudden change of refractive index, which is called “Fresnel reflection,” can be avoided, and the antireflection effect in such SWS can be achieved.<sup>[109,121–123]</sup>

Various antireflective nanoarray structures have been particularly designed to increase light absorption.<sup>[117,124,125]</sup> Such antireflective structures are broadband, quasi-omnidirectional, and intrinsically more stable than multilayer antireflection coatings since no foreign materials are involved, resulting in higher light absorption as well as better stability for artificial photosynthesis.<sup>[92,104,126]</sup> For example, a tapered Si nanohole (SiNH) array photocathode with a gradient refractive index has been developed via a metal-assisted electroless etching method for PEC water splitting.<sup>[92]</sup> This tapered SiNH array can simulate multiple dielectric layers to match the optical impedance, as the effective refractive index of each layer changes gradually along the direction of the SiNH depth (Figure 3c), resulting in a superior broadband antireflection. Furthermore, the antireflection properties of this structure are mainly determined by the total etching depth of the tapered SiNHs. Although the specular reflection originated from the smooth surface decreases significantly with increasing hole depth, the diffuse reflection from the rough surface increases. For this reason, the etching depth of SiNHs is optimized to ≈400 nm to minimize both types of reflection for increased light absorption compared to the planar counterpart. Due to the addition of tapered SiNHs, the photocurrent density is improved by ≈30% ( $\approx 33 \text{ mA cm}^{-2}$ ) compared to a planar counterpart ( $\approx 25 \text{ mA cm}^{-2}$ ), while the overpotential required for H<sub>2</sub> evolution was reduced.

Although some progress has been made, the development of antireflective nanoarrays used for artificial photosynthesis is limited by traditional synthesis methods and mechanisms. To further increase light absorption, rationally designed antireflective nanoarrays based on advanced synthesis methods (e.g., 3D printing) and new mechanisms (e.g., plasmonic antireflective surfaces) can be considered.

## 2.3. Slow Light Effect

Before introducing the slow light effect exhibited by nanoarray structures of photonic crystal on increase of light absorption,

some important definitions are given. Photonic crystals are periodic ordered nanostructures composed of two constituents, one with a lower refractive index (RI) and the other with a higher RI;<sup>[127–129]</sup> it can forbid the propagation of light in a certain crystal direction within a certain spectrum regime, called a photonic stop-band.<sup>[96]</sup> Furthermore, the periodic RI structure affects the group velocity ( $v_g$ ) of light in a manner as described by Equation (12)<sup>[130,131]</sup>

$$v_g = d\omega/d\kappa = \frac{c}{n + \omega \frac{dn}{d\omega}} \quad (12)$$

where,  $c$ ,  $\omega$ ,  $n$ , and  $\kappa$  represent the speed of light, light frequency, refractive index, and wave vector, respectively. If the RI changes dramatically at the interface between the high and low RI dielectrics ( $dn/d\omega \gg 1$ ), the group velocity of light will tend to be zero, and this light is referred as slow light. Slow light in photonic crystals undergoes strong coherent multiple scattering and travels with a very low velocity near the photonic stop-band edges,<sup>[95,131,132]</sup> which enables storage of light in the photonic crystal. The basic idea is that if light could reside in the material for a longer period of time, the interaction between matter and light would be enhanced, resulting in increased light absorption.<sup>[127,133]</sup>

The photoelectrodes with 3D photonic crystal structures, mainly semiconductor IOs, have been applied for both water splitting<sup>[134–136]</sup> and CO<sub>2</sub>RR.<sup>[74,137]</sup> Taking the WO<sub>3</sub> photoanode with an IO structure (Figure 3d) prepared by the forced impregnation approach for PEC water splitting as an example, the light absorption as well as photocurrent density (a maximum of 100% increase) can be remarkably enhanced when the edge of the photonic stop-band of WO<sub>3</sub> IOs overlaps with the absorption edge of WO<sub>3</sub>, compared to that with a disordered porous structure, owing to the slow light effect in IOs.<sup>[96]</sup>

## 2.4. Surface Plasmon Resonance

SPR, which is the incident photon-induced resonant oscillation of conduction electrons in the metal,<sup>[99,138–141]</sup> exists mainly in two distinct forms: i) localized SPR (LSPR) with nonpropagating, collective oscillation of the surface electrons in metal nanostructures and ii) surface plasmon polariton (SPP) propagating at the metal/dielectric interface.<sup>[20,105]</sup> SPR effect is often induced in semiconductors to enhance light absorption.<sup>[142–145]</sup> Noble metals (e.g., Au and Ag), non-noble metals (e.g., Al and Cu), as well as transparent conductive metal oxides (e.g., In-doped SnO<sub>2</sub>, ITO) have been reported for realizing of SPR effect.<sup>[105,146–150]</sup> For plasmonic nanostructure arrays, there are at least three ways for light absorption enhancement.<sup>[49]</sup> First, the metallic nanoparticles decorated on the arrays can act as subwavelength scattering elements to couple and trap incident light by confining the incident light into the nanoarray structure. Second, the metallic nanoparticles decorated on the array structures can also be used as subwavelength antennas, in which the plasmonic near-field is coupled to the semiconductor, resulting in the increase of absorption cross-section. Third, a corrugated metallic film on the back surface of a light

active nanoarray can couple light into SPP modes supported at the metal/nanoarray interface as well as guided modes in the nanoarray, whereupon the light is converted to photocarriers.

Since the plasmonic structures have many advantages for enhanced light absorption, they have been widely used in artificial photosynthesis.<sup>[151–154]</sup> For instance, an array of hematite nanorods within a plasmonic Au nanohole (Figure 3e), fabricated by nanosphere lithography and hydrothermal method, significantly improves the light absorption by putting together the synergistic effects of LSPR and SPP.<sup>[105]</sup> In the long-wavelength region, the LSPR mode increases the absorption across the entire spectral range of hematite owing to LSPR absorption of the Au nanohole array (the peak is centered at 650 nm), as revealed from UV-visible absorption spectra in Figure 3f. In the short-wavelength region, the extraordinary transmission of the SPP modes concentrates the incident light at the energies above the band edge of hematite. The nanorods are similar to miniature optical fibers, which trap the incident light and enhance the light absorption of hematite. By combining the LSPR and SPP effects, enhanced light absorption over a broad spectral range is achieved for the hematite nanorod–Au nanohole array, resulting in increased IPCE value (Figure 3g) and an approximately tenfold increase in the photocurrent at a bias of 0.23 V versus Ag/AgCl under simulated sun irradiation. So far, the pioneered reports on surface plasmon resonance have been mostly based on noble metals. It is significant to develop the non-noble metal-based nanoarrays with strong surface plasmon resonance, low cost and excellent stability. Furthermore, the development of theoretical calculation is needed in the future to delicately design/optimize the size, shape, spacing, and orientation of desired plasmonic nanoarray structures before experiment.

## 2.5. Bandgap Narrowing

Many wide bandgap semiconductors such as TiO<sub>2</sub> and ZnO (both with bandgaps >3.0 eV) are potentially interesting for artificial photosynthesis as these are highly stable and low cost materials. However, their extremely limited response toward the visible light results in poor light absorption as well as low efficiency.<sup>[98,107,155]</sup> In order to improve the solar energy conversion efficiency of these wide bandgap semiconductors, bandgap narrowing has been reported, where light absorption is increased by broadening the absorption spectrum.<sup>[156–158]</sup>

Various methods for narrowing bandgap of semiconductors to increase light absorption include doping with donors/acceptors, introducing vacancies or defects and developing various solid solutions.<sup>[59,158–160]</sup> Doping donors/acceptors as well as introducing vacancies or defects is carried out to create localized states in the bandgap to promote light absorption.<sup>[106,161,162]</sup> For example, Yang et al. prepared nitrogen-doped ZnO nanowire arrays combining a hydrothermal method and annealing for PEC water splitting.<sup>[59]</sup> The introduction of N in the crystal lattice of ZnO results in an intermediate energy level in the bandgap and narrows the bandgap from 3.3 eV (pristine ZnO) to the visible region (N-doping ZnO), thus improving the light collection in the visible region. In addition, Kang et al. prepared reduced TiO<sub>2</sub> NTAs with oxygen vacancies

used as a photoanode for PEC water splitting.<sup>[106]</sup> As shown in the UV-visible–near infrared (NIR) diffuse reflectance spectra (Figure 3h), the pristine TiO<sub>2</sub> NTAs are only active under UV irradiation while the photoresponse of reduced TiO<sub>2</sub> NTAs is effectively extended into the visible and NIR regions owing to the existence of oxygen vacancy. As a result, the bandgap of reduced TiO<sub>2</sub> NTAs is narrowed from 3.09 eV (pristine TiO<sub>2</sub> NTAs) to 2.46 eV, enhancing light absorption as well as the photocurrent (from 0.193 to 0.732 mA cm<sup>-2</sup> at 1.23 V<sub>RHE</sub>).

Although doping is effective in bandgap narrowing, the use of a single dopant can cause charged defects due to charge compensation, which act as recombination centers and shorten carrier lifetime, thereby limiting the catalytic efficiency of the material.<sup>[163]</sup> Another method, which applies passive donor–acceptor codoping to form a solid solution, can not only reduce the bandgap but also avoid charge recombination owing to the relatively lower donor–acceptor charge compensation,<sup>[163]</sup> and it has been applied for nanoarray structures to improve light absorption for solar energy conversion.<sup>[100,164–166]</sup> Abbas et al. developed a facile chemical vapor deposition method for preparing a photoanode constituted by 3D branched nanowire (3D B-NW) arrays of ZnO–GaN:ZnO for PEC water splitting.<sup>[100]</sup> This ZnO–GaN:ZnO 3D B-NW photoanode offers two absorption edges: the first edge at about 409.2 nm (3.03 eV) corresponds to the doping of N atoms into crystal lattice of ZnO causing a red shift in its absorption edge, while the second at 500 nm (2.48 eV) is attributed to the bandgap absorption of GaN:ZnO solid solution. As a result, the bandgap of this solid solution nanoarray is narrowed and thus the light absorption is enhanced.

## 2.6. Photosensitizer Decoration

Decorating photosensitizers on nanoarray structures is another approach<sup>[107]</sup> to enhance light absorption in an extended spectrum range for solar energy conversion.<sup>[103,158]</sup> Various types of photosensitizers such as quantum dots (QDs) and metal–organic frameworks (MOFs) have been used in this field.

For QDs, carbon quantum dots (CQDs), including graphene quantum dots (GQDs), are very promising because they are environmentally friendly, nontoxic, earth-abundant and have broadband optical absorption and chemical stability, as well as being amenable to facile large-scale production at low cost.<sup>[102,107,167–171]</sup> Zhang et al. reported the preparation of a CQDs/TiO<sub>2</sub> nanotube array photoanode, which combines electrochemical etching and anodization methods, for PEC hydrogen generation.<sup>[107]</sup> In this configuration (Figure 3i), CQDs display strong absorption of sunlight in a broad spectral range from the ultraviolet to the NIR region. Diffused reflectance UV-visible spectra shows that the reflectance of CQDs/TiO<sub>2</sub> NTs anode is lower than the unsensitized anode in the 410 and 900 nm wavelength range, resulting in higher light absorption. Furthermore, compared to pristine TiO<sub>2</sub> NTs, only the CQD-sensitized TiO<sub>2</sub> NTs photoanode exhibits a positive IPCE value in the visible region.<sup>[101]</sup> Therefore, decorating with CQDs can extend the light response range of TiO<sub>2</sub> NTs from UV to the visible as well as NIR regions, and thus achieve an over sixfold increase in photoconversion efficiency. Similarly, GQDs can

also be utilized as a photosensitizer on the ZnO nanorod arrays to enhance light absorption.<sup>[172]</sup> In addition, narrow-gap semiconductor QDs, such as CdS,<sup>[63,173]</sup> CdSe,<sup>[174]</sup> and CdTe,<sup>[64]</sup> are also used as photosensitizers on nanoarrays to enhance light absorption.

Recently, MOFs with highly ordered skeletal structures and large surface areas have also shown their unique properties as photosensitizers: first, MOFs can regulate their optical and catalytic properties on a molecular scale, which is beneficial to both light absorption and catalytic reactions; second, the highly porous structure of MOFs can also be used to incorporate other functional molecules (such as molecular catalysts) to improve the photocatalytic efficiency synergistically.<sup>[103]</sup> For example, Ti-based MOFs have proven to be promising photosensitizers for PEC water splitting.<sup>[103]</sup> After amine modification to narrow the bandgap of MOFs, the TiO<sub>2</sub>/MOF nanowire array presents obvious red-shift in light absorption toward visible light compared to the pristine TiO<sub>2</sub> nanowire array. Therefore, it is expected that a large number of MOFs with different light absorption wavelengths can be used as promising photosensitizers for solar energy conversion.

## 2.7. Hybrid Structures

To achieve higher performance in light absorption, there have been several reports on hybrid nanoarray structures that combine two or more of the above described strategies to show synergistic effects.<sup>[151]</sup> For example, Chen et al. fabricated an antenna/spacer/reflector-based Au-surface/BiVO<sub>4</sub>/WO<sub>3</sub>/Au-bottom nanopatterned via a template-assisted method for water splitting.<sup>[108]</sup> In this complex nanoarray structure, two strategies for enhancing light absorption are presented (Figure 3j). First, a large ( $\approx$ 245 nm) Au NSs bonded to the Au-bottom film can scatter incident light in the backward direction as a reflector. The integration of BiVO<sub>4</sub> into the nanopatterned Au-bottom film not only increases the surface roughness factor, but also achieves a dual light capture strategy, resonant light trapping and light retrapping. Second, for the small ( $\approx$ 20 nm) Au-surface NSs decorated on the BiVO<sub>4</sub>, the light absorption effect is dominant compared to the light scattering effect, which enables light harvesting of both the incident and reflected light from the Au bottom. Thus, this hybrid structure can concentrate light energy in the spacer (BiVO<sub>4</sub> layer) and promote light trapping and absorption of BiVO<sub>4</sub>, resulting in a photocurrent density of 1.31 mA cm<sup>-2</sup> at 1.23 V<sub>RHE</sub>, which demonstrates an impressive 3.23-fold enhancement compared to the bare BiVO<sub>4</sub>.

Nanoarrays have been demonstrated to be an efficient structure for improving light absorption in artificial photosynthesis. Various light management strategies (e.g., multiple light scattering, antireflection, slow light effect, SPR, bandgap narrowing, and photosensitization) have been realized through well-designed nanoarrays with high uniformity and tunable patterns, which are able to increase the light absorption intensity and/or extend the spectral range. However, using one of the above strategies can only achieve limited increase in light absorption, which is far from satisfactory to meet the practical need for artificial photosynthesis. In the long term, the rational design of hybrid nanoarray structures that should be

focused on owing to its synergistic effect on light absorption enhancement.

## 3. Charge Transport and Transfer

Simulations have suggested, by taking TiO<sub>2</sub> as a model catalyst, that the key to enhance the photocatalytic efficiency is to increase the concentration of surface-reaching photoholes before reaching the threshold instead of the intrinsic catalytic activity of TiO<sub>2</sub>.<sup>[175]</sup> Both calculation and experimental results demonstrate that the interfacial charge transfer rate plays a dominant role in determining the photocatalytic activity of the CdS/reduced graphene oxide (RGO) model heterojunction. The interfacial electron/hole transfer rate is a product of the surface free electron/hole concentration and the effective single electron/hole transfer probability, both of which are associated with the surface potential.<sup>[176]</sup> Thus, it is reasonable to conclude that charge transport and transfer is significant to achieving high efficiency in artificial photosynthesis.<sup>[35,82]</sup> In this section, two categories, including single- and dual-bandgap nanoarray structures, will be summarized for promoting charge transport and transfer.

### 3.1. Single-Bandgap Nanoarray Structures

Taking the n-type semiconductor as a working electrode in the PEC system (Figure 4a),<sup>[177]</sup> single-bandgap nanoarray structures exhibit the ability to decouple the light absorption length along the long axis from the hole collection distance in the orthogonal axis, and favor the collection of electrons to the substrate through a direct pathway, thus achieving higher solar-to-fuel conversion efficiency than the thin film counterpart. This suggests that using a single-bandgap nanoarray structure is an effective strategy to promote charge transport.<sup>[27,179]</sup>

For example, a vertically oriented graphite carbon nitride (g-CN) porous nanorod (PNR) array photoanode has been synthesized by thermal polycondensation of cyanimide precursors using anodic aluminum oxide (AAO) as a template (Figure 4b).<sup>[57]</sup> Compared to the g-CN nanoparticle film (NPF), the confinement effect of the AAO template increases the number of  $-\text{NH}-$  hole-accepting defect sites at the atomic scale and the degree of  $\pi$ -electron conjugation of the aromatic ring at the molecular scale in the g-CN PNR, thus promoting exciton dissociation and increasing the electron mobility in the bulk, respectively.<sup>[57]</sup> Furthermore, this PNR array (Figure 4c) provides an increased specific surface area to facilitate mass transfer at the solid/solution interface, a shortened pathway for the electron transport from the material to the substrate and an enlarged SCR relative to the bulk to facilitate charge separation at the material surface compared to the NPF.<sup>[27,57]</sup> As a result, the g-CN PNR array photoanode affords an over four times charge separation efficiency than that of the NPF at 1.23 V<sub>RHE</sub> (Figure 4d), and thus shows an outstanding PEC performance among the g-CN-based polymer photoanodes without any sacrificial reagents. This work highlights the role of nanoarray structures in promoting charge separation, transport, and transfer.

To further improve the efficiency of solar energy conversion, introducing appropriate amount of dopants, defects,

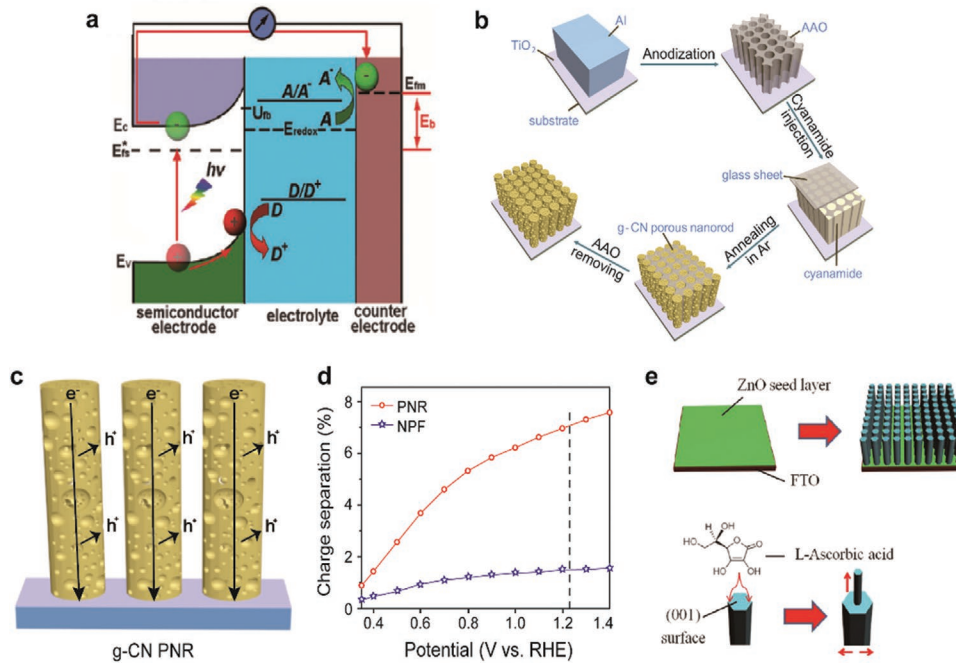


**Figure 4.** a) Schematic band diagrams illustrating PEC process: a bare n-type semiconductor under light irradiation with external bias. Reproduced with permission.<sup>[177]</sup> Copyright 2015, Royal Society of Chemistry. Schematic diagrams showing b) the procedure for fabricating a g-CN PNR array photoanode and c) the pathways of charge transport in g-CN PNR. d) Charge separation efficiencies of g-CN PNR and NPF (the dashed line shows the charge separation efficiency at 1.23 V<sub>RHE</sub>). Reproduced with permission.<sup>[57]</sup> Copyright 2018, American Chemical Society. e) Schematic of the formation process of ZnO nanopencil arrays. Reproduced with permission.<sup>[178]</sup> Copyright 2014, Elsevier Ltd.

and vacancies into single-bandgap nanoarray structures can increase the charge carrier density to improve electrical conductivity and then further promote charge transport.<sup>[155,178,180–183]</sup> For instance, Lv et al. fabricated aligned ZnO nanopencil arrays with oxygen vacancies by an aqueous chemical method, in order to solve the rapid charge recombination problem of pristine ZnO (Figure 4e).<sup>[178]</sup> The electrochemical impedance measurement proves that the enhancement of carrier density in the ZnO nanopencil arrays can be attributed to the oxygen vacancies, which can prohibit the electron–hole recombination by trapping the photogenerated electrons, assisting the transfer of the holes to the ZnO/electrolyte interface for OER. The key point is that the amount of dopants, defects, and vacancies should be controlled properly, since excessive of them may turn into charge recombination sites and lower the charge separation efficiency, leading to decreased solar energy conversion efficiency.<sup>[184,185]</sup>

### 3.2. Dual-Bandgap Nanoarray Structures

Forming dual-bandgap (heterojunction and homojunction) nanoarray structures that combine advantages of the two constituents has been recognized as another attractive method for promoting charge transport.<sup>[47,186–188]</sup> In addition to having the advantages mentioned above for single-bandgap nanoarray structures, dual-bandgap nanoarray structures can also promote charge separation to minimize the energy-wasteful electron–hole recombination owing to the built-in electric field formed at the interfacial region of two constituents.<sup>[176,189,190]</sup> Compared

to the single-bandgap systems, dual-bandgap systems with an ideal theoretical efficiency of 41% are more likely to achieve the minimum efficiency requirement of 10% for practical solar water splitting.<sup>[176]</sup> Therefore, extensive efforts have been made to develop different types of dual-bandgap systems, as shown below.

#### 3.2.1. Heterojunctions

Heterojunction nanoarray structures formed between two solid materials, such as semiconductor–semiconductor (SC–SC) and semiconductor–metal (SC–M) heterojunction nanoarrays, are among the most widely used structures in artificial photosynthesis as shown in Figures 5–7.<sup>[25,191]</sup>

**Semiconductor–Semiconductor Heterojunctions:** Compared to single-bandgap systems, SC–SC heterojunctions can suppress charge recombination due to the built-in electric field formed by equilibration of the individual Fermi levels. This results in more efficient charge separation, longer charge carrier lifetimes, and higher reaction rates.<sup>[191,192]</sup> As shown below, the SC–SC heterojunction nanoarray structures are generally classified into Type II, Z-scheme, and ferroelectric polarization three categories according to their different charge transport pathways and mechanisms.

**Type II:** In a typical Type II structure, a staggered band alignment is formed, where the positions of CB and VB of semiconductor 1 are higher than those of semiconductor 2, as shown in Figure 5a. After contact, the photogenerated electrons from the higher CBM of semiconductor 1 migrate to the lower CBM

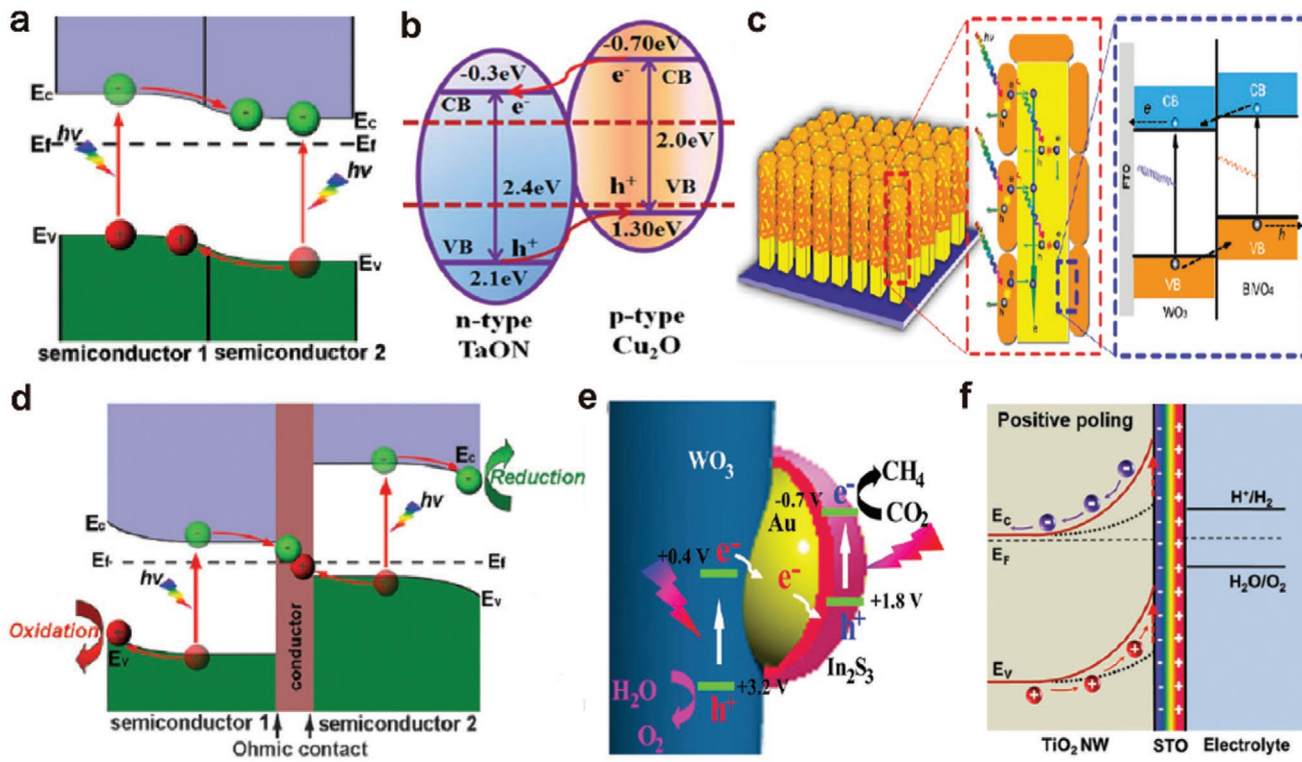


**Figure 5.** a) Schematic band diagram illustrating the Type II SC-SC heterojunction. Reproduced with permission.<sup>[177]</sup> Copyright 2015, Royal Society of Chemistry. b) Energy band structure of the p-Cu<sub>2</sub>O/n-TaON nanorod array photoanode. Reproduced with permission.<sup>[193]</sup> Copyright 2014, Royal Society of Chemistry. c) Schematic illustration and energy band structure of the WO<sub>3</sub>/BiVO<sub>4</sub> nanorod array photoanode. Reproduced with permission.<sup>[44]</sup> Copyright 2011, American Chemical Society. d) Schematic band diagrams illustrating an SC-conductor-SC all-solid-state Z-scheme structure. Reproduced with permission.<sup>[177]</sup> Copyright 2015, Royal Society of Chemistry. e) Schematic illustration of the charge separation and transfer in the Z-scheme system of WO<sub>3</sub>/Au/In<sub>2</sub>S<sub>3</sub>. Reproduced with permission.<sup>[194]</sup> Copyright 2016, American Chemical Society. f) Schematic electronic band diagram of the TiO<sub>2</sub>-STO interface under positive poling condition. Reproduced with permission.<sup>[195]</sup> Copyright 2017, Wiley-VCH GmbH.

of semiconductor 2; while the photogenerated holes are transported from the lower VBM of semiconductor 2 to the higher VBM of semiconductor 1. As a result, band bending occurs in the SCR, which creates a built-in electric field and thus facilitates the charge separation at the interface, followed by further charge transfer toward bulk semiconductors, driven by their potential difference. A Type II junction consisting of n-type and p-type semiconductors (p-n junctions) provides better performance than two identical types (two n-types or p-types) of semiconductors because of the larger difference in work functions and potentials between the different types of semiconductors.<sup>[177]</sup> And three typical Type II SC-SC heterojunction nanoarrays will be introduced below.

One typical Type II structure is called p-n heterojunction.<sup>[196–199]</sup> When such a structure is irradiated by photons with energy higher than or equal to the bandgaps of the semiconductors, the built-in electric field can direct the flow of electrons from the CB of the p-type material to that of the n-type material and the holes can move from the VB of the n-type material to that of the p-type material.<sup>[25]</sup> The p-Cu<sub>2</sub>O/n-TaON nanorod array, fabricated by hydrothermal method and a chemical bath deposition process, is one of the typical p-n heterojunction nanostructures used in PEC water splitting (Figure 5b).<sup>[193]</sup> This heterojunction nanostructure shows better performance compared to the single TaON photoanode owing to effective

charge separation: the potential difference between p-Cu<sub>2</sub>O and n-TaON causes electrons from Cu<sub>2</sub>O to collect toward the Ta substrate, while holes from TaON migrate to the surface of Cu<sub>2</sub>O to take part in chemical reactions.<sup>[193]</sup> In addition, the unique 1D nanorod array structure promotes electron collection to the substrate and also provides abundant surface reaction sites owing to its 1D conductive electron transport “highway” and large specific surface area, respectively, thereby leading to water oxidation with high performance.

In addition, two identical types (two n-types or p-types) can also form Type II structures for promoting charge transport and transfer.<sup>[200,201]</sup> The WO<sub>3</sub>/BiVO<sub>4</sub> nanorod array photoanode is an example of two n-type semiconductors (Figure 5c), where the CBM of WO<sub>3</sub> is lower than that of BiVO<sub>4</sub>, electrons in the CB of BiVO<sub>4</sub> can transfer to that of WO<sub>3</sub>. Likewise, since the VBM of WO<sub>3</sub> is lower than that of BiVO<sub>4</sub>, holes in the VB of WO<sub>3</sub> transfer to that of BiVO<sub>4</sub>, thus making efficient charge separation at the interface of the WO<sub>3</sub>/BiVO<sub>4</sub> heterojunction. Here too, the WO<sub>3</sub>/BiVO<sub>4</sub> nanorod array provides electrons a direct transport path to the substrate and shortens the distance (orthogonal to the nanorods) for holes to reach the electrolyte for oxidation reaction. As a result, the WO<sub>3</sub>/BiVO<sub>4</sub> photoanode that integrates heterojunction structures into 1D nanorod arrays, promotes charge-carrier separation and transfer.<sup>[44,202]</sup> And, a hybrid CuO-Cu<sub>2</sub>O nanorod array, which

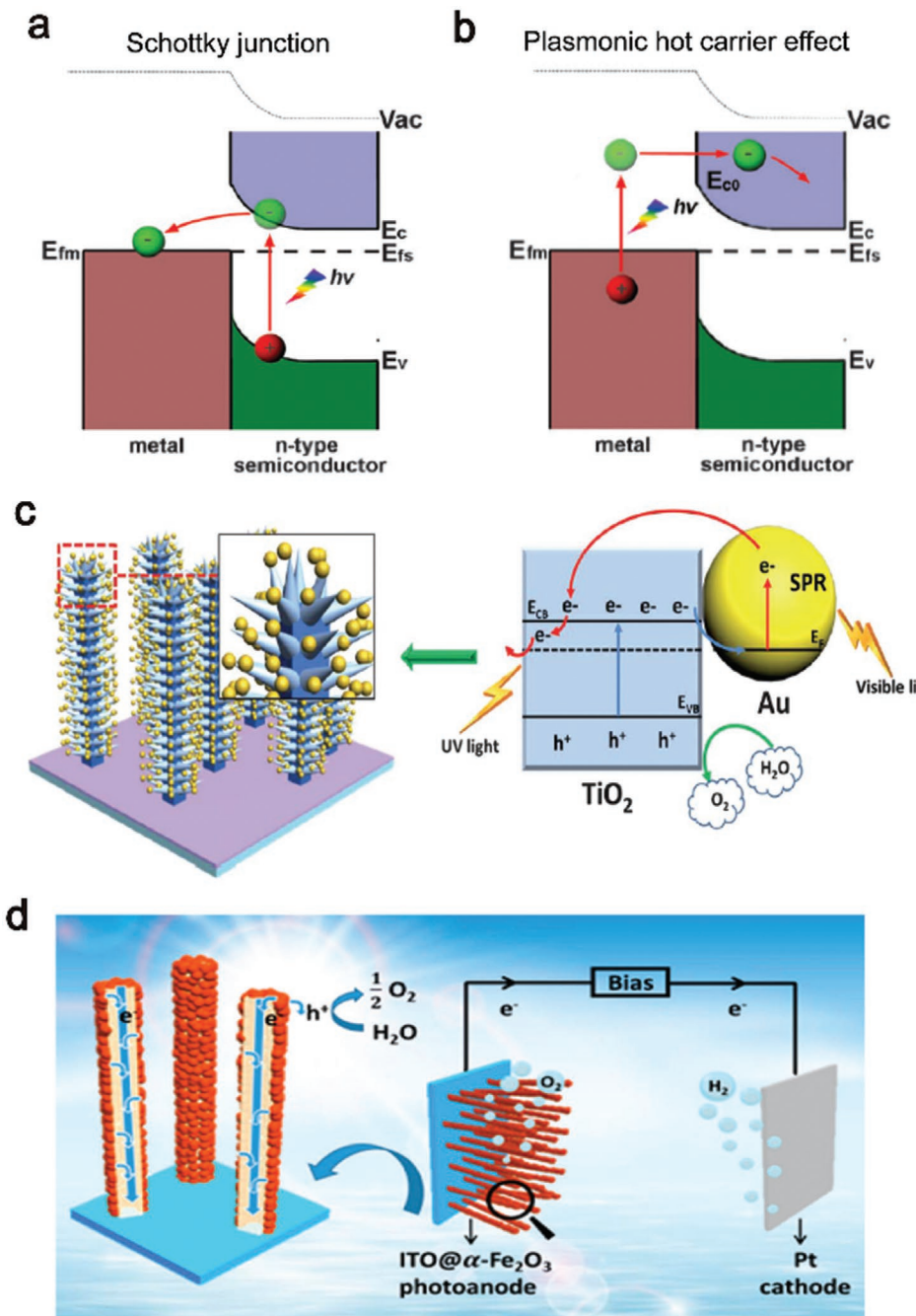


**Figure 6.** Schematic illustrating the processes of charge separation and transfer driven by the a) Schottky junction or b) plasmonic hot carrier effect between a metal and an n-type semiconductor. Reproduced with permission.<sup>[177]</sup> Copyright 2015, Royal Society of Chemistry. c) Charge transfer mechanism between Au nanoparticles and TiO<sub>2</sub> in visible and UV light. Reproduced with permission.<sup>[212]</sup> Copyright 2013, Royal Society of Chemistry. d) Schematic illustration of ITO@ $\alpha$ -Fe<sub>2</sub>O<sub>3</sub> core–shell nanowire arrays working as a photoanode for PEC water splitting. Reproduced with permission.<sup>[213]</sup> Copyright 2015, American Chemical Society.

is used as a photocathode for CO<sub>2</sub>RR, shows a Type II configuration in the case of two p-type semiconductors.<sup>[203]</sup> Owing to the potential difference of the two oxides, the transfer of photogenerated electrons from Cu<sub>2</sub>O to CuO is promoted for reactions while holes are collected to the substrate, and thus achieve better PEC performance compared to the single Cu<sub>2</sub>O photoelectrode.

**Z-Scheme:** Another SC–SC heterojunction system is Z-scheme (Figure 5d), which is composed of two different semiconductors combined with an electron mediator.<sup>[177]</sup> In such a system, an electron mediator (e.g., a conductor or interfacial defects) exist at the contact interface of the two semiconductors, which can form an ohmic contact between the electron mediator and the semiconductors with low contact resistance.

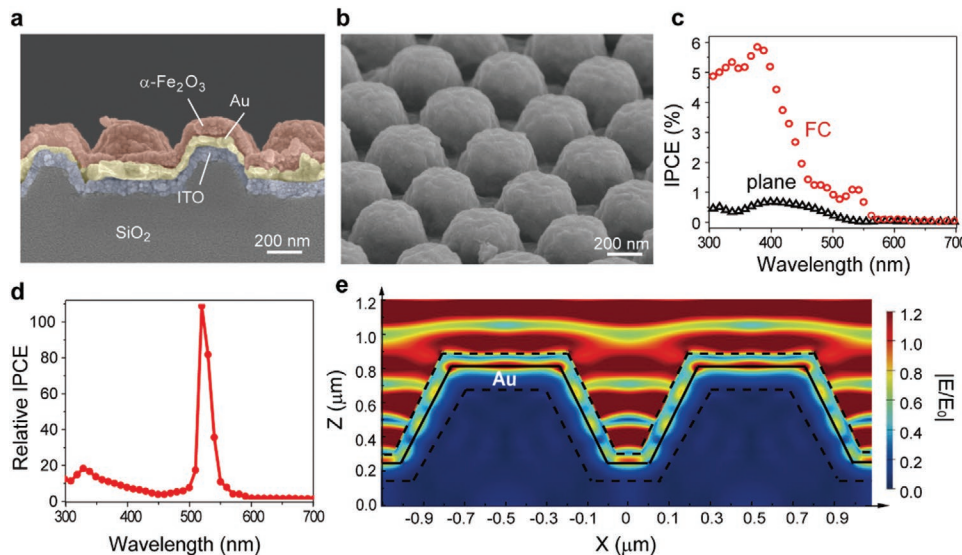


**Figure 7.** a) Cross-sectional and b) tilted SEM images of the  $\text{SiO}_2/\text{ITO}/\text{Au}/\alpha\text{-Fe}_2\text{O}_3$  anode with the FC nanograting structure. c) Spectrally resolved IPCE curves of the FC nanograting and planar structures of  $\text{SiO}_2/\text{ITO}/\text{Au}/\alpha\text{-Fe}_2\text{O}_3$  in the wavelength range of 300–700 nm at 1.23 V<sub>RHE</sub>. d) Relative IPCE curve of the  $\text{SiO}_2/\text{ITO}/\text{Au}/\alpha\text{-Fe}_2\text{O}_3$  photoanode with the FC nanograting structure, calculated by dividing its IPCE by that of the planar sample. e) FDTD-simulated electric field  $|E/E_0|$  distribution of FC nanograting structures of  $\text{SiO}_2/\text{ITO}/\text{Au}/\alpha\text{-Fe}_2\text{O}_3$  at the wavelength of 516 nm. Reproduced with permission.<sup>[219]</sup> Copyright 2019, American Chemical Society.

As shown in Figure 5d, the photogenerated electrons from the lower CBM of semiconductor 1 can directly recombine with the photogenerated holes from the higher VBM of semiconductor 2 through the ohmic contact. In addition, the electrons in the higher CBM of semiconductor 2 and the holes in the lower VBM of semiconductor 1 will be preserved for the reduction and oxidation reactions, respectively. In particular, the Z-scheme system can possess strong redox ability since the remaining electrons and holes well maintain their energy levels so that the reaction activities will not be compromised.<sup>[177,204,205]</sup>

Taking the  $\text{WO}_3/\text{Au}/\text{In}_2\text{S}_3$  nanowire array, where the conductor Au is the electron mediator, as an example for Z-scheme (Figure 5e), the photogenerated electrons from the lower CBM of  $\text{WO}_3$  would recombine with the holes from the higher VBM of  $\text{In}_2\text{S}_3$ , with the help of Au at the interface. At the same time, the photogenerated electrons left in the CB of  $\text{In}_2\text{S}_3$  and the holes remaining in the VB of  $\text{WO}_3$  can be used for reduction and oxidation half reactions, respectively, constituting an overall redox reaction.<sup>[194]</sup> As a result, prolonged lifetime of charge carriers and enhanced charge separation efficiency are achieved in the  $\text{WO}_3/\text{Au}/\text{In}_2\text{S}_3$  nanowire array, benefiting for the charge transport. Similar Z-scheme nanoarray structures, such as  $\text{Fe}_2\text{V}_4\text{O}_{13}/\text{RGO}/\text{CdS}$  nanoribbon array<sup>[206]</sup> and  $\text{BiVO}_4/\text{C}/\text{Cu}_2\text{O}$  nanowire array,<sup>[207]</sup> have also been reported for  $\text{CO}_2\text{RR}$  with enhanced charge separation efficiency.

In addition, since a large number of defects exist at the SC–SC interface, which are the centers for charge recombination and thus can play a similar role in the conductor–semiconductor ohmic contact,<sup>[177,204]</sup> the Z-scheme nanoarray structures of the direct contact between two semiconductors without a conductor can also be applied for PEC water splitting as well as  $\text{CO}_2\text{RR}$ , such as the bird-nest structured  $\text{ZnO}/\text{TiO}_2$  photoanode,<sup>[208]</sup> the  $\text{WO}_3/\text{Cu}_2\text{O}$  nanorod photoanode,<sup>[209]</sup> and the  $\text{CuFeO}_2/\text{Nb-doped TiO}_2$  nanotube photocathode.<sup>[210]</sup> However,

its higher electrical resistance hinders the faster charge transfer compared to that with a conductor, so the further optimization is needed in this system.

**Ferroelectric Polarization:** Ferroelectric semiconductors, such as  $\text{BiFeO}_3$  (BFO) and  $\text{SrTiO}_3$  (STO), can combine with other semiconductors to regulate their band structures and promote charge transport,<sup>[195,211]</sup> by using the phenomenon of ferroelectric polarization.<sup>[47]</sup> The spontaneous electric polarization induces considerable free charge redistribution in adjacent semiconductors, through which, the amplitude of the SCR can be effectively tuned (Figure 5f).<sup>[195]</sup> Ferroelectric polarization can increase the amplitude of interfacial band bending to promote charge separation and migration, and also lower charge recombination.<sup>[47]</sup> For example, the simultaneous enhancement of charge separation and transport by making use of ferroelectric polarization in  $\text{TiO}_2\text{-STO}$  core–shell nanowire arrays, which are fabricated by a two-step hydrothermal method, has been reported.<sup>[195]</sup> The STO shell with controllable thickness leads to considerable spontaneous polarization in the positive poling direction and effectively amplifies electrical band bending of  $\text{TiO}_2$ . As a result, the ferroelectric STO thin shell significantly improves charge separation efficiency with minimal influence on the hole-migration property of the  $\text{TiO}_2$  photoelectrodes, leading to a dramatic increase in photocurrent density. However, the ferroelectric material with strong ferroelectric polarization used at present are all wide bandgap ( $>3$  eV) semiconductors with low charge mobility. It is thus desired to develop new semiconducting ferroelectric materials with higher electron mobility, which can allow enhanced charge separation at the interface and fast transportation through the ferroelectric material simultaneously for the further improved ferroelectric-polarization-related PEC performance.

**Semiconductor–Metal Heterojunctions:** Besides SC–SC heterojunctions, the semiconductor–metal (SC–M) heterojunction is

a commonly used configuration to promote charge transport. Taking an n-type semiconductor as an example, in terms of interfacial charge transfer, there are mainly two mechanisms involved in SC–M heterojunctions: the Schottky junction (Figure 6a) and the plasmonic hot carrier effect (Figure 6b). In addition, materials with high conductivity can be used as conductive scaffolds for promoting current collection and transport.<sup>[47]</sup>

**Schottky Junction:** A Schottky junction is a heterostructure produced by the direct contact of a metal with a semiconductor. Both metal and semiconductor have a work function ( $W$ ), which corresponds to the minimum energy required to remove electrons from the Fermi level ( $E_F$ ) to the vacuum level ( $V_{ac}$ ). Using an n-type semiconductor as an example, we assume that the Fermi level of the metal ( $E_{fm}$ ) is lower than that of the semiconductor ( $E_{fs}$ ) before their contact (i.e.,  $W_m > W_s$ ). After they intimately contact with each other (Figure 6a), in order to establish an equilibrium state between  $E_{fs}$  and  $E_{fm}$ , electrons of the semiconductor diffuse to the metal at a lower energy level (causing accumulation of negative charges), and holes stay in the VB of the semiconductor (causing accumulation of positive charges). As a result of the diffusion process, free electrons in the semiconductor near the SC–M interface are depleted compared to those in the bulk, and a SCR is formed at the surface of the semiconductor. This causes the upward band bending from the semiconductor to the metal, forming a Schottky barrier.<sup>[177]</sup> In a word, following excitation of the semiconductor, the metal effectively acts as an electron trap to receive photoelectrons from the semiconductor, thus improving charge carrier separation and reducing recombination in SC–M heterojunctions.<sup>[25,191]</sup>

Some SC–M nanoarray structures have applied the above mechanism in solar energy conversion. For example, TiO<sub>2</sub> branched nanorod arrays (TiO<sub>2</sub> BNRs) with Au nanoparticles (Figure 6c, left part) fabricated by Su et al. prove that Schottky junction can promote charge separation at the TiO<sub>2</sub>/Au interface.<sup>[212]</sup> Under UV light illumination, TiO<sub>2</sub> is photoexcited to generate electrons and holes, and the photogenerated electrons presented in the CB of TiO<sub>2</sub> are transferred to the surface of Au nanoparticles. Due to the different work functions of Au and TiO<sub>2</sub>, a Schottky barrier is created as a trap for electrons, reducing the recombination of electron–hole pairs and thus keeping holes in the VB of TiO<sub>2</sub> for oxidation reaction (Figure 6c, blue lines in the right part). Other cases such as Au–Cu/graphene/Cu<sub>2</sub>O nanowire arrays<sup>[214]</sup> and Pd/TiO<sub>2</sub> nanowire arrays,<sup>[215]</sup> also show the advantage of Schottky junction in charge separation at the SC–M interface.

**Plasmonic Hot Carrier Effect:** In addition to the light absorbing function mentioned in Section 2.4, plasmonic effect can also be exploited for promoted charge transfer by hot carrier injection (Figure 6b).<sup>[177]</sup> In the case of an n-type semiconductor combined with a plasmonic metal, under light irradiation, conduction electrons in the plasmonic metal are excited to become highly energetic electrons (known as “hot electrons”). When the energy of the hot electrons is higher than the flat-band CB potential (CB level before the band bending) of the neighboring semiconductor, they can escape from the plasmonic metal and transfer directly into the CB of the semiconductor.

The Au/TiO<sub>2</sub> BNRs mentioned in 3.2.1.2.1, also show plasmonic hot carriers effect owing to the presence of plasmonic

Au.<sup>[212]</sup> In the visible region, hot electrons generated from the SPR excitation of Au nanoparticles are injected to the CB of the TiO<sub>2</sub> BNRs (Figure 6c, red lines in the right part). After going through the 1D nanorod structure, these electrons are collected to the FTO substrate, and finally transferred to the Pt counter electrode for HER. Similar structures such as Au/TiO<sub>2</sub> nanotube arrays,<sup>[97]</sup> Au/ZnO nanowire arrays,<sup>[98]</sup> ZnO/Au/CdS IOs,<sup>[135]</sup> and Ag–Ag<sub>2</sub>S/TiO<sub>2</sub> nanotube arrays<sup>[216]</sup> also promote charge transport and transfer owing to the plasmonic hot carriers effect. Current research shows that utilizing the hot carrier injection mechanism to promote charge transfer can only result in very limited improvement in the photosynthesis efficiency. Hence, more effort is needed to combine plasmonic hot carrier effect with other charge transfer improvement effects to maximize the photosynthesis efficiency of the SC–M nanoarray structure.

**Conductive Scaffold:** A special type of SC–M nanoarray structure is obtained by using specific materials with metallic-like high conductivity to replace metals, including TiSi<sub>2</sub>, graphene, FTO, ITO, and AZO, as conductive scaffolds for improvement of charge transport.<sup>[47,213,217,218]</sup> Taking  $\alpha$ -Fe<sub>2</sub>O<sub>3</sub> as a model metal oxide system, short diffusion length and low electronic conductivity in charge transport are the two main drawbacks in this system. To tackle these problems, highly conductive ITO nanowire arrays with outstanding electronic conductivity ( $\approx 500 \text{ S cm}^{-1}$ ) are combined with the  $\alpha$ -Fe<sub>2</sub>O<sub>3</sub> to form the ITO@ $\alpha$ -Fe<sub>2</sub>O<sub>3</sub> core–shell nanowire array photoanode (Figure 6d).<sup>[213]</sup> In such a structure, the “core” ITO nanowire array with high conductivity not only links with  $\alpha$ -Fe<sub>2</sub>O<sub>3</sub> via a chemical bath deposition method without any obvious impurity or amorphous layer, which benefit the transfer of electrons from  $\alpha$ -Fe<sub>2</sub>O<sub>3</sub> to ITO, but also provides a direct pathway for electron collection to the substrate. Thus, ITO is demonstrated to be a suitable scaffold that enables efficient charge transport and transfer in the photoanode and improves its PEC performance.

**Light-Induced Electric Field:** SPR can also induce electric field in semiconductors to promote charge transport besides the hot carrier effect mentioned in 3.2.1.2.2. For instance, the well-defined periodic frustum of a cone (FC) nanograting of the SiO<sub>2</sub>/ITO/Au/ $\alpha$ -Fe<sub>2</sub>O<sub>3</sub> photoanode has been fabricated successfully (Figure 7a,b), where the SPP-induced electric field in hematite plays a dominant role in efficiency enhancement by facilitating charge separation, thus dramatically increasing the IPCE by more than 2 orders of magnitude at the near bandgap of hematite (Figure 7c,d).<sup>[219]</sup> In this architecture, the SPP-induced electric field (Figure 7e) can be evanescent into dielectric materials up to approximately half the involved wavelength,<sup>[220]</sup> which is larger than the charge collection distance ( $L+W$ ) in  $\alpha$ -Fe<sub>2</sub>O<sub>3</sub>, leading to more effective separation of photogenerated charge carriers. Furthermore, compared to other built-in electric field produced at the interface of heterojunctions, the SPP-induced electric field can be created in the single material to facilitate the charge separation, bypassing the common problems of interfacial charge recombination due to great disparity in composition and lattice constant, or band misalignment between different SC materials. In addition to the SPP effect at the near bandgap of  $\alpha$ -Fe<sub>2</sub>O<sub>3</sub>, this nanoarray photoelectrode with a nonplanar Au back contact has photonic light scattering,<sup>[221]</sup> which can induce an electric

field in the middle of the  $\alpha\text{-Fe}_2\text{O}_3$  layer in a much broader spectral region.<sup>[222]</sup> This electric field is also closely related to the OER activity. In a word, this example shows a precise control of the electric field distribution by facile modulation of the nanoarray structures to promote charge transport in solar energy conversion.

### 3.2.2. Homojunctions

Although forming heterojunctions has been proved to be an effective strategy to induce built-in electric fields, most of them have some disadvantages, such as the abrupt composition change, which might cause charge recombination and poor stability at the interface.<sup>[223–225]</sup> To overcome these problems, researchers have proposed homojunctions with homogeneous elemental composition. A vertically aligned nanosheet-array-like BiOI homojunction consisting of BiOI nanosheets and microplates (MPs), has been prepared for photocatalytic HER.<sup>[226]</sup> Since nanosheet and MP have different sizes, an effective BiOI@BiOI homojunction with Type II staggered band energy levels can be formed, where a built-in electric field is induced at the interface that reduces the barrier for charge transfer and suppresses the recombination of photogenerated electrons and holes, thereby promoting photocatalytic activity.

However, the above-mentioned homojunction provides interfacial electric fields that are only active around the interface and cannot benefit the separation of electrons and holes generated in the bulk region. Regarding to this issue, the zinc-blend (ZB)–wurtzite (WZ) homojunction superlattice structure (**Figure 8a,b**) was prepared by a solvothermal method, to improve the charge separation in the entire semiconductor crystals.<sup>[227]</sup> In this architecture, ZB and WZ have same composition, great lattice match at their homointerface along the [111-0001] orientation, and the staggered type II band alignment between ZB and WZ allotropes, which facilitate the interfacial charge transfer. More importantly, the WZ structure shows spontaneous polarization along the [0001] orientation, whereas the ZB structure is polarization-free due to the highly symmetric atom arrangement.

As a result, a saw-tooth-like potential profile forms along the [111-0001] orientation in the ZB–WZ superlattice (**Figure 8c**), thus driving the photogenerated electrons and holes to separate and accumulate alternatively at the ZB–WZ interfaces.<sup>[228]</sup> The theoretical simulation proves the existence of the saw-tooth-like potential profile and demonstrates that the intensities and distribution of the built-in electric fields in adjacent ZB and WZ segments can be tuned by changing the specific configuration of the ZB–WZ superlattice (**Figure 8d**).<sup>[227]</sup> Compared to the limited built-in electric field distribution formed in the conventional junction structure, the saw-tooth-like electric field formed in the ZB–WZ superlattice structure is more widely distributed throughout the entire bulk region in many II–IV, III–V, and IV group semiconductors, having a great potential in high-efficiency charge separation and utilization.

It is worth noting that great progress has been achieved in the study of nanoarrays for charge transport and transfer. n-Type (or p-type) nanoarrays themselves can decouple the light absorption length along the long axis from the hole (or electron) collection distance in the orthogonal axis, and favor the collection of electrons (or holes) to the substrate through a direct pathway. Furthermore, doping and forming dual-bandgap (heterojunction and homojunction) can further promote charge transport and transfer by improved electrical conductivity and built-in electric field, respectively. Nevertheless, limitations (e.g., electric resistance and instability) related to the interfacial connection between two constituents still need to be emphasized for dual-bandgap nanoarrays, since they are not conductive to promoting charge transport. Material selection and fabrication method should be further optimized in the future study to obtain more stable and lower-resistance dual-bandgap nanoarrays.

## 4. Catalytic Reaction

Redox reactions in artificial photocatalysis occur at the catalyst/electrolyte interface. The two factors, kinetics and selectivity, influence the reaction efficiency and the yield of the specific

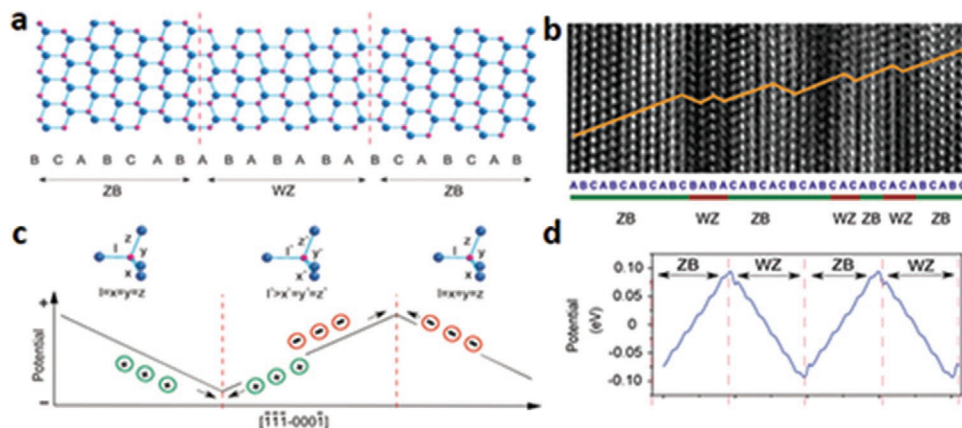


**Figure 8.** a) Atomic model and b) high-resolution transmission electron microscopy (HRTEM) image of ZB–WZ superlattice structure. Purple and blue balls in (a) represent cations and anions, respectively. c) Spontaneous polarization-induced saw-tooth-like potential profile along the [111-0001] direction. d) DFT calculation of electrostatic potential profiles of the ZB–WZ superlattice. The potential distribution in the ZB–WZ superlattice can be tuned by changing its specific configuration. Reproduced with permission.<sup>[227]</sup> Copyright 2017, Elsevier Ltd.

fuels. In this section, various nanoarrays are introduced to regulate these two factors, respectively.

#### 4.1. Kinetics

Semiconductor photoabsorbers (PAs) usually show slow kinetics in artificial photosynthesis. Modification of ECs on the PA surface<sup>[229–231]</sup> plays an important role in reducing the overpotential and accelerating the reaction kinetics.<sup>[232–234]</sup> However, parasitic light absorption occurs since ECs deposited on the PA surface are usually opaque. Therefore, a trade-off between light absorption and catalytic activity in PA/EC hybrid systems always exists in solar energy conversion.

Spatially separating light absorption from catalytic reaction is a promising way to alleviate their contradiction. Hence, one feasible way is irradiation of PAs on the opposite side of the EC coating, which allows the light absorption and redox reaction to occur in different regions. Besides, nanoarray structure-based ECs and PAs with large specific surface area, which are conducive to increasing the number of active sites and the loading of ECs, leading to the acceleration of kinetic process.<sup>[235,236]</sup> Both cases of irradiation of PAs on the opposite and same sides of the EC coating with featured nanoarray structures will be elaborated in the following section.

##### 4.1.1. Irradiation of Photoabsorbers on the Opposite Side of Electrocatalyst Coating

One way to balance light absorption and catalytic activity is irradiation of PAs on the different side of EC coating (back-irradiation). This back-irradiation configuration allows the deposited ECs with large surface area and thick enough, providing a great number of active sites without compromising light absorption by PAs. Taking a back-irradiated Si-based photoanode, which integrates the polycrystalline n<sup>+</sup>p-Si and NiFe-layer double hydroxide (LDH) nanosheet array (**Figure 9a**) with a partially activated Ni (Ni/NiO<sub>x</sub>) as a bridging layer, as an example (**Figure 9b**),<sup>[233]</sup> the NiFe-LDH nanosheet array structure can be sufficiently thick for abundant active sites to reduce

the OER overpotential. This system exhibits an onset potential of 0.78 V<sub>RHE</sub> and a photocurrent density of  $\approx$ 37 mA cm<sup>-2</sup> at 1.23 V<sub>RHE</sub> for OER (**Figure 9c**), which is the benchmark activity reported so far for crystalline Si-based photoanodes.<sup>[237]</sup> This back-irradiation provides an alternative system configuration to achieve high PEC activity by coupling a large number of efficient OER or HER ECs with PAs.

##### 4.1.2. Irradiation of Photoabsorbers through Electrocatalyst Coating

For irradiation of PAs through the EC coating, two strategies have been devised to address the trade-off between light absorption and catalytic activity, including patterning EC arrays on the PA plane and loading ECs on the surface of PA arrays. The following section shall put light on these strategies in detail.

*Planar Photoabsorbers with Electrocatalyst Arrays:* For a PA/EC system with a planar PA, constructing patterned ECs on the PA surface is a promising way to decouple light absorption from catalytic activity. In such a configuration (**Figure 10a**), the production of fuels or chemicals occurs on the ECs surface. Light can only be absorbed by the uncovered region of the PA since ECs are usually opaque and have thicknesses of over dozens of nanometers that makes it difficult for light to pass through the ECs to reach the PA.<sup>[238,243]</sup> Consequently, the size, morphology, and coverage of the patterned ECs on the PA surface are crucial to balance the light absorption and catalytic activity, which is highly affected by the exposed areas of both PAs and ECs.

Patterned ECs on the PA surface are usually fabricated by photolithography. By using different photomasks, the coverage of the patterned ECs on the PA surface can be tuned, which is of significance to the device performance. Taking the patterned Ti/Pt EC on a STO-modified Si photocathode as a model system (**Figure 10b**),<sup>[238]</sup> Ji et al. concluded that tuning the sizes of ECs to be smaller than the limiting factors such as diffusion length and SCR width would greatly increase the applied bias photon to current efficiency. Besides water splitting, the patterned ECs have also been applied to achieve high-performance CO<sub>2</sub>RR. Song et al. developed a Si photoelectrode system with the mesh-type cocatalyst for oxygen reduction reaction (ORR) (**Figure 10c**).<sup>[239]</sup> The incident light can be absorbed by Si

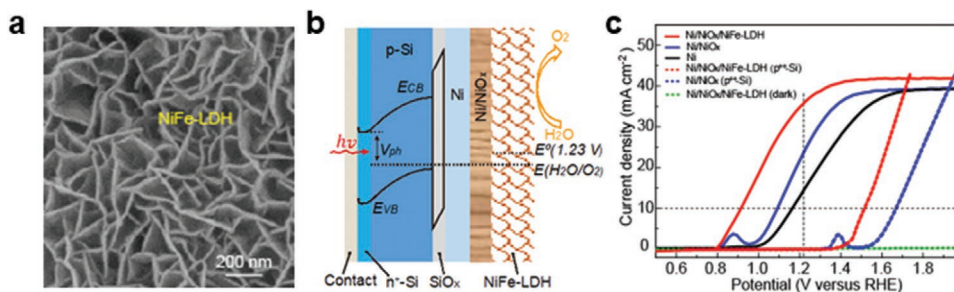


**Figure 9.** a) Top-view SEM image of NiFe-LDH. b) Schematic of the cross-section and energy band alignment of the designed multicomponent n<sup>+</sup>p-Si/SiO<sub>x</sub>/Ni/NiO<sub>x</sub>/NiFe-LDH photoanode for water oxidation. c) PEC performance of photoanodes. J-V behavior of Ni/NiO<sub>x</sub>/NiFe-LDH (under illumination, red solid curve; in the dark, green dashed curve), Ni/NiO<sub>x</sub> (blue solid curve), Ni (black solid curve) coated n<sup>+</sup>p-Si/SiO<sub>x</sub> anodes, and Ni/NiO<sub>x</sub>/NiFe-LDH (red dashed curve) and Ni/NiO<sub>x</sub> (blue dashed curve) coated nonphotoactive p<sup>++</sup>-Si electrodes (here the degenerate p<sup>++</sup>-Si simply acts as a conductive substrate). Vertical and horizontal black dashed lines are for the convenience of comparison of the water oxidation activities of all the electrodes at the equilibrium potential for water oxidation and the potential needed to reach the current density of 10 mA cm<sup>-2</sup>. Reproduced with permission.<sup>[233]</sup> Copyright 2018, American Chemical Society.

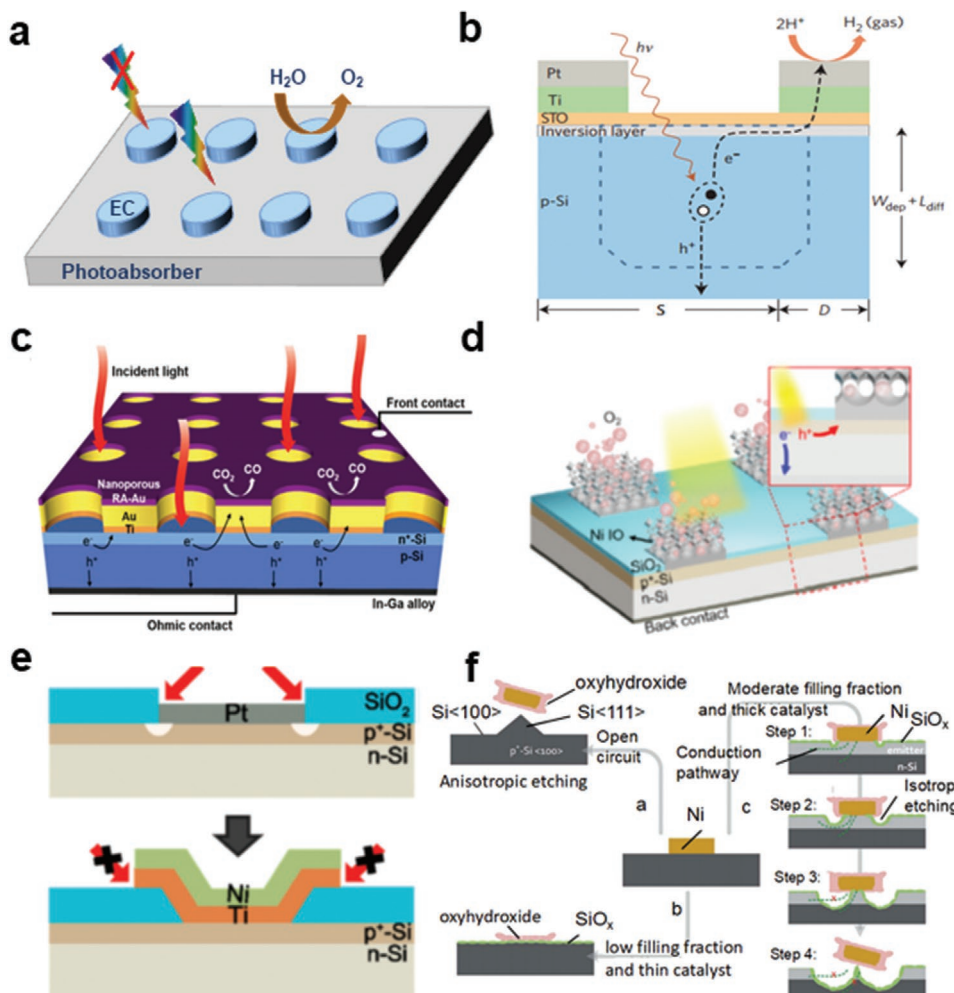


**Figure 10.** a) Schematic illustration of a PA coupled with patterned ECs. b) Schematic plot of Si/STO/Ti/Pt photocathode.  $S$ ,  $D$ ,  $W_{\text{dep}}$ , and  $L_{\text{diff}}$  represent spacing, diameter, SCR width, and the diffusion length of electrons, respectively. Reproduced with permission.<sup>[238]</sup> Copyright 2014, Springer Nature. c) Schematic of a Si photoelectrode with Au mesh cocatalysts design for CO<sub>2</sub>RR. Reproduced with permission.<sup>[239]</sup> Copyright 2016, Wiley-VCH GmbH. d) Schematic design of oxide-passivated p<sup>+</sup>-Si photoanode with micropatterned Ni IOs. Reproduced with permission.<sup>[240]</sup> Copyright 2017, American Chemical Society. e) Schematic diagram of the local dissolution mechanism for a Si photoanode with Pt catalyst and that with modified Ni and Ti to eliminate the dissolution paths. Reproduced with permission.<sup>[241]</sup> Copyright 2015, American Chemical Society. f) Schematic of failure-process pathways for Si photoelectrode coupled with Ni island during OER in 1 M KOH. Reproduced with permission.<sup>[242]</sup> Copyright 2018, Royal Society of Chemistry.

through the circular openings to provide photovoltage and the nanoporous cocatalyst with mesh-type exhibits favorable catalytic activity of CO<sub>2</sub> reduction to CO, which contribute to the excellent PEC CO<sub>2</sub>RR with over 90% Faradaic efficiency of the CO<sub>2</sub>-to-CO conversion at the CO<sub>2</sub>/CO equilibrium potential.

In addition to these single PAs coupled with ECs system, Chen et al. quantitatively analyzed the solar to hydrogen conversion efficiency ( $\eta_{\text{STH}}$ ) of tandem PAs with patterned ECs by experiment and simulation.<sup>[243]</sup> They found that the  $\eta_{\text{STH}}$  is closely related to the filling fraction ( $f_c$ , also named coverage ratio) and the bandgap of the tandem PAs. Specifically, in the case of the ECs with very low  $f_c$  ( $<0.01$ ), the high bandgap combinations are required to drive the water-splitting reaction with such low filling-fraction films. A further decrease in the  $f_c$  results in a significant drop in  $\eta_{\text{STH}}$  due to the rapid increase of the kinetic overpotential overwhelms the reduction in the parasitic absorption. When the  $f_c$  of ECs increases beyond

0.01, the  $\eta_{\text{STH}}$  exhibits a weak dependence on the  $f_c$  of the ECs, because the reduction of the kinetic overpotential allows the use of tandem PAs with smaller bandgap combinations with increasing filling fraction, and thus yields higher optimal operating current densities that compensate for the increase in the parasitic light absorption of the EC. These studies reveal that an optimal  $f_c$  of the ECs and bandgap of PAs is necessary to acquire high hydrogen conversion efficiency since it is tightly associated with both light absorption and catalytic activity.

Compared to the common EC patterns mentioned above, the EC patterns with ordered 3D porous nanostructures, such as IOs, provide a higher surface area, which means that coating PA partially by a 3D EC pattern could provide more active sites with the same  $f_c$  of ECs on the PA surface. For example, Oh et al. prepared a Si photoanode patterned with NiFe alloy IO nanostructure (Figure 10d).<sup>[240]</sup> The obtained photoanode shows a high PEC OER performance with an onset potential

of  $0.94 \text{ V}_{\text{RHE}}$  and photocurrent density of  $31.2 \text{ mA cm}^{-2}$  at  $1.23 \text{ V}_{\text{RHE}}$ , which is better than that of the photoanode with planar ECs.

It should be noted that the patterned ECs also influence the stability of a photoelectrode. It is important to understand the mechanism underlying corrosion of a photoelectrode with patterned ECs so as to develop effective strategies to improve its stability. Taking the Si photoanode with micropatterned Pt as a model system, Oh and Oh found that the dissolution of Si easily occurs at the edge of Pt, which is caused by the penetration of the corrosive electrolyte through the interface/gap between the  $\text{SiO}_2$  and the Pt, or through pinholes in the Pt film.<sup>[241]</sup> It is possible to mitigate this local Si dissolution by blocking the corrosion pathways, which can be achieved by extending the coverage of the ECs to overlap the  $\text{SiO}_2$  surface as shown in Figure 10e. Subsequently, Sun et al. investigated the failure mechanism for the Si photoanodes with different  $f_c$  of ECs.<sup>[242]</sup> They revealed that the corrosion initiates at the edges of the Ni islands for the photoanode with moderate  $f_c$  and thick ECs (Figure 10f). Under continued operation, the etching of the Si surface is aggravated, eventually resulting in the detachment of the ECs. Further study on more materials shows that the failure of the photoanodes with low  $f_c$  or thin ECs occurs due to the conversion of ECs into porous structures during the OER operation. These results indicate that the corrosion usually initiates at the edges of activated catalysts for the photoelectrode with patterned ECs, which provides a hit about how to design photoelectrodes with high stability.

**Photoabsorber Arrays with Electrocatalyst Coating:** Besides patterning EC arrays on the PA plane, loading ECs on the surface of PA arrays such as micro- and nanowire arrays also have been widely adopted in artificial photosynthesis.<sup>[61,247,248]</sup> In such a system, the PA arrays can provide large surface area, which contributes to increasing the loading of ECs and light absorption relative to the plane PA. Herein, the PA arrays with fully and partially ECs coating in the field of artificial photosynthesis will be introduced. The core–shell structure photoelectrode with the PA array surface fully covered with ECs is widely applied in artificial photosynthesis, in which the PA array core and the EC shell are responsible for light absorption and catalysis respectively. In the core–shell structure, more attention should be paid on the optical transparency and thickness of the ECs shell to ensure sufficient light absorption and the EC activity. Jin and co-workers reported a 3D p-Si/NiCoSe<sub>x</sub> core–shell nanopillar array photocathode for hydrogen production. The synergic effects of the light harvesting of the Si array core and the good optical transparency and electrocatalytic activity of the NiCoSe<sub>x</sub> shell boost the production and utilization of photogenerated electrons, resulting in an enhanced PEC HER performance.<sup>[45]</sup> For those opaque ECs such as Ni(OH)<sub>2</sub> and NiFe-LDH deposited on the PA array surface, an adverse parasitic light absorption will be produced. Thus, an optimal thickness of ECs is needed to balance the light absorption of the underlying PA arrays and catalytic activity.<sup>[249,250]</sup> He and co-workers disclosed that the PEC OER performance of the  $\text{WO}_3@\text{NiFe-LDH}$  nanorod array increases with increasing NiFe-LDH deposition time and then decreases for prolonged deposition time.<sup>[250]</sup> The excess deposition of NiFe-LDH may lead to the formation of the densely packed NiFe-LDH layer, which hinders both absorp-

tion of light and prompt transfer of photogenerated holes to the reactive interface.

The other kind of structure is the PA array with partially coated ECs. In such a structure, ECs are loaded at the top or bottom of the micro- and nanowires, providing a convenient way to decouple light absorption from catalytic activity. In this case, the catalytic reactions and light absorption are carried out on the surface of PA arrays with and without EC coverage, respectively, achieving spatial separation. For instance, the Ni–Mo nanopowder was deposited at the base of a high-aspect-ratio n<sup>+</sup>p-Si microwire array and covered with a TiO<sub>2</sub> light-scattering layer to achieve efficient water reduction (Figure 11a).<sup>[244]</sup> The mass loading of Ni–Mo at the bottom of the n<sup>+</sup>p-Si microwire serves to reduce the HER overpotential. Furthermore, the TiO<sub>2</sub> layer scatters light back into the Si microwire, allowing light to pass through the Si microwire array several times, thus increasing light absorption. Further, Vijselaar et al. investigated the influence of the pitch of the microwires and the EC coverage ratio on PEC water splitting performance.<sup>[245]</sup> Their results indicate that for photocathodes with the low microwire pitch and high  $f_c$  of ECs (upper left corner of Figure 11b), the overall device HER efficiency ( $\eta$ ) is predominantly governed by light absorption. Conversely, for photocathodes with the high microwire pitch and low  $f_c$  of ECs, the  $\eta$  is limited by the amount of the active catalyst (lower right corner of Figure 11b). Between the two extremes, a region of optimal performance is found, where both catalytic activity and light absorption are optimized (red region in Figure 11b). These studies demonstrate that partial loading of ECs on PA arrays is an effective way to decouple light absorption from catalytic activity. Besides loading the ECs on PA arrays directly, Lin et al. developed a conducting polymer (CP) (Figure 11c) that fills in the intervals of PA arrays, providing large surface area to load ECs particles, thus contribute to an increased active sites.<sup>[246]</sup> Moreover, this CP matrix with large surface area also allows uniform dispersion of the ECs particles without aggregation, thus reducing the parasitic light absorption caused by ECs aggregation. Besides, this CP matrix can also facilitate the charge separation and transport, which is conducive to an advanced PEC water splitting performance.

## 4.2. Catalytic Selectivity

During the solar energy conversion process such as CO<sub>2</sub>RR, a variety of carbon-based fuels can be produced through different reduction pathways. In addition, the competitive reactions such as the reactive oxygen species generation during water splitting, the HER during CO<sub>2</sub>RR and NRR will also affect the yield of the desired product. Therefore, the catalytic selectivity is a key issue that needs to be addressed for obtaining the desired product with high yield. In this section, two different hybrids including PA/EC (refer to abiotic ECs here) and PA/enzyme structures have been summarized for improving catalytic selectivity.

### 4.2.1. Photoabsorber/Electrocatalyst Hybrid Arrays

ECs immobilized on the surface of the PA can not only accelerate the surface reaction kinetics but also improve the catalytic

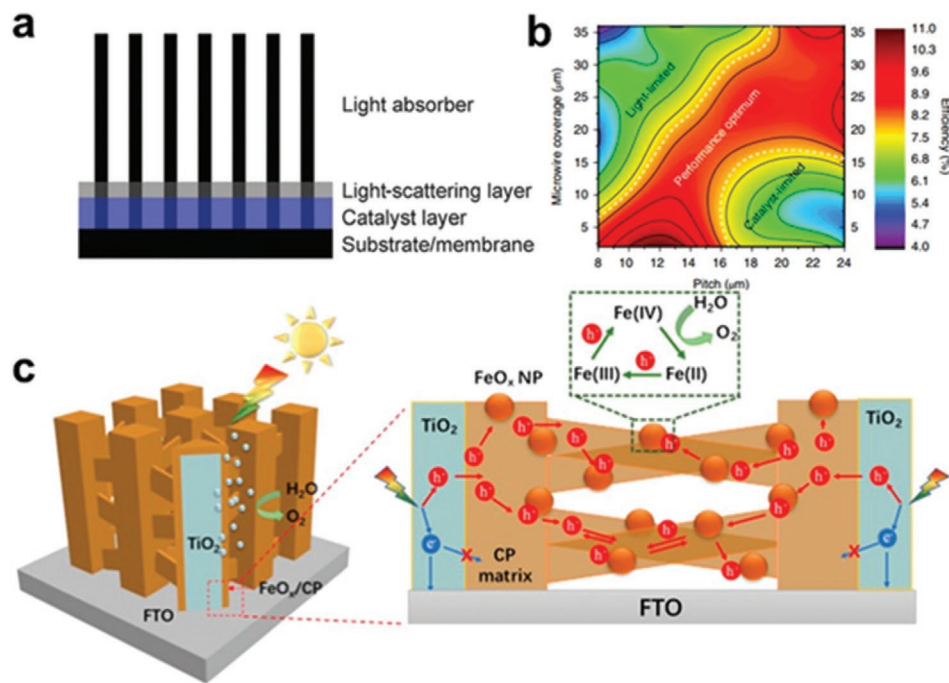


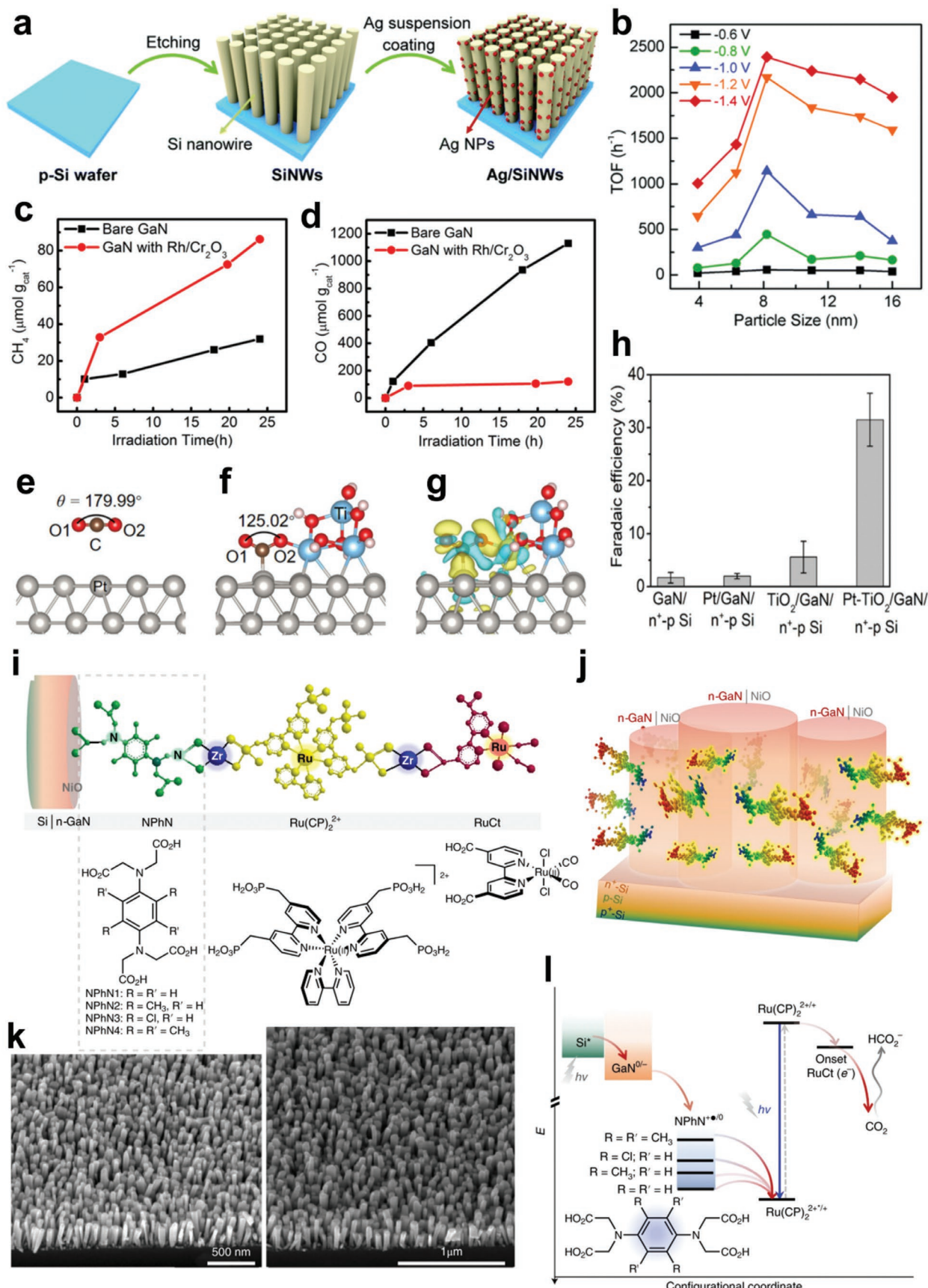
**Figure 11.** a) Schematic of a photocathode based on arrays of Si microwires. Reproduced with permission.<sup>[244]</sup> Copyright 2015, Royal Society of Chemistry. b) Contour plot of the overall device HER efficiency,  $\eta_{\text{HER}}$ , as a function of the pitch and wire coverage for all tested combinations. Reproduced with permission.<sup>[245]</sup> Copyright 2018, Springer Nature. c) Schematic of the CP- $\text{FeO}_x/\text{TiO}_2$  photoanode showing the crosslinked  $\text{FeO}_x$ -CP/ $\text{TiO}_2$  network in between the arrayed  $\text{TiO}_2$  nanorods. Reproduced with permission.<sup>[246]</sup> Copyright 2019, American Chemical Society.

selectivity.<sup>[255]</sup> Here, we focus mainly on the influence of ECs on the catalytic selectivity of  $\text{CO}_2$  reduction considering its significance in addressing energy security and environmental issues.<sup>[256]</sup> For the metal ECs/PA arrays, their catalytic selectivity was found to be improved by altering the size and structure of metal ECs. For instance, the Ag/SiNW catalysts (Figure 12a) with smaller AgNPs not only have a larger specific surface area for  $\text{CO}_2$  reduction but also own stronger CO adsorption strength.<sup>[251]</sup> Therefore, among the Ag/SiNW catalysts with different size of AgNPs (4.2, 6.3, 8.2, 11, 14, and 16 nm), the Ag-8.2/SiNW with a sufficient specific surface area and appropriate CO adsorption shows the best  $\text{CO}_2$ -to-CO catalytic activity (Figure 12b).<sup>[251]</sup> With regard to the structure-dependent  $\text{CO}_2$ RR, the Au nanowire exhibits a better catalytic activity of  $\text{CO}_2$ -to-CO than the Au nanoparticle because of the higher fraction of CO-evolving edge sites on the Au nanowire.<sup>[257]</sup> Another commonly used ECs for the construction of ECs/PA arrays is the metal/oxide structure. On the GaN nanowire arrays, an increased product selectivity of  $\text{CH}_4$  over CO can be achieved after depositing Rh/Cr<sub>2</sub>O<sub>3</sub> core/shell nanoparticles (Figure 12c,d) owing to the effective CO adsorption on the Cr<sub>2</sub>O<sub>3</sub> facilitating its further reduction to  $\text{CH}_4$ .<sup>[252]</sup> When loaded Pt-TiO<sub>2</sub> on their surface, the main product of  $\text{CO}_2$ RR is CO considering that the metal/oxide interface (Pt-TiO<sub>2</sub> as a model) can spontaneously activate  $\text{CO}_2$  and stabilize the key reaction intermediates for facilitating CO production (Figure 12e-h).<sup>[253]</sup> This interfacial effect is also found on the Cu NP decorated Co<sub>3</sub>O<sub>4</sub> nanotube array electrode, which displays a nearly 100% catalytic selectivity for  $\text{CO}_2$ -to-formate conversion.<sup>[258]</sup> For this electrode, the positive surface charge at the Cu/Co<sub>3</sub>O<sub>4</sub> interface enhances the  $\text{CO}_2^-$  adsorption and the subsequent protonation of reduction

intermediates, thus resulting in high catalytic selectivity toward  $\text{CO}_2$ -to-formate. Apart from the metal/oxide ECs, the molecular p-n-junction assembly ( $\text{Ru}(\text{CP})_2^{2+}$ -RuCl) can also be functionalized onto the semiconductor p-n-junction (n-GaN nanowire arrays on the n<sup>+</sup>-p-p<sup>+</sup> silicon substrate, Si|n-GaN) to form a binary molecular-semiconductor p-n junctions for  $\text{CO}_2$ RR (Figure 12i-k).<sup>[254]</sup> Light absorption by the molecular assembly results in a redox-separated state of the molecular assembly that accepts the electrons from the photoexcited Si|n-GaN due to the lower CB of the molecular assembly as compared with that of n-GaN, which sustains  $\text{CO}_2$  reduction at the molecular assembly and depresses water reduction at Si|n-GaN (Figure 12l). Therefore, the catalytic selectivity of  $\text{CO}_2$ RR toward HER increases when the surface coverage of the molecular assembly is increased properly.<sup>[254]</sup> In another research, the cobalt-containing zeolite imidazolate framework (ZIF9)/Co<sub>3</sub>O<sub>4</sub> nanowire array interface was constructed, which also shows a nearly 100%  $\text{CO}_2$ -to-fomate catalytic selectivity in liquid products.<sup>[259]</sup> This high selectivity is ascribed to the following reasons: 1) preferred binding to  $\text{CO}_2$  on ZIF9 than water leads to an enhanced  $\text{CO}_2$  surface concentration; 2)  $\text{CO}_2$  can be activated after being adsorbed on ZIF9-Co<sub>3</sub>O<sub>4</sub> NWs, which lowers the  $\text{CO}_2$  reduction overpotential and increases kinetics of  $\text{CO}_2$  reduction than water/proton reduction on the active sites.<sup>[259]</sup>

#### 4.2.2. Photoabsorber/Enzyme Hybrid Arrays

In comparison with inorganic ECs, enzymes as naturally derived biocatalysts have more complex catalytic centers which



not only contain amino acid residues to provide electrostatic and hydrogen bonding interactions with substrates and to stabilize intermediates, but also offer redox-active cofactors and locally hydrophobic pockets to facilitate charge transfer, resulting in a much higher catalytic efficiency and selectivity. However, in the enzyme-based biological photosynthetic systems, the limited light absorption of photosystem (PS) I/II and the priority of optimization of survival strategies result in low solar-to-biomass conversion efficiencies.<sup>[266,267]</sup> Therefore, construction of PA/enzyme hybrids by combining the advantages of inorganic array structures in light absorption, charge transport and transfer, and reaction kinetics with high catalytic efficiency of enzymes is expected to overcome limitations in natural and artificial photosynthetic systems to achieve both high selectivity and high efficiency in artificial photosynthesis.<sup>[268,269]</sup>

So far, three types of PA/enzyme hybrid arrays with increasing levels of complexity have been reported. For the first type, single enzymes are directly immobilized on PA surfaces. For instance, the hydrogenase ( $H_2$ ase) or the nitrogenase molybdenum–iron protein functionalized onto PAs such as Ru dye-sensitized  $TiO_2$  NPs and  $CdS$  nanorods have been reported for the photocatalytic HER and NRR, respectively.<sup>[270–272]</sup> Likewise, the  $O_2$ -evolving PSII loaded on the hematite nanorod and on the porous  $TiO_2$  nanotube network-modified ITO electrodes (Figure 13a) have been designed for the photocatalytic OER.<sup>[260,273]</sup> In this PSII-based hybrid, PSII not only functions as an OER catalyst but also plays a complementary role to PA in light harvesting. Inspired by these two separated systems for HER and OER, a light-driven photobiological water splitting system under the applied bias is built up by directly coupling of PSII–IO-mesoITO (ITO with a macroporous IO architecture and a mesoporous skeleton) with the  $H_2$ ase–IO-mesoITO (Figure 13b).<sup>[261]</sup> Considering the low reduction potential and the limited light absorption of PSII, the diketopyrrolopyrrole dye sensitized  $TiO_2$ , which provides a sufficient potential to reduce protons when using the  $H_2$ ase–IO-ITO electrode and has complementary absorption to PSII, is introduced to prepare a PSII–dye sensitized IO- $TiO_2$ / $H_2$ ase–IO-ITO PEC cell that functions at zero bias.<sup>[274]</sup> However, the slow interfacial electron transfer between the PA surface and the electrostatically bound enzyme as well as the instability of the enzyme greatly affects their performance. To address these issues, the

second type of the PA/enzyme hybrid system was developed by indirectly coupling PA array structures such as QD-sensitized  $TiO_2$  nanotube (Figure 13c),<sup>[262]</sup> ordered carbon nitride (CNA) (Figure 13d,e),<sup>[263]</sup> and SiNW arrays (Figure 13f)<sup>[264]</sup> with dehydrogenase enzymes using the coenzyme photoregeneration property of PAs. In all these hybrid systems, the PA arrays are able to regenerate coenzyme nicotinamide adenine dinucleotide (NADH) under light irradiation, which acts as an electron donor in the enzymatic reduction reactions such as  $CO_2$ RR for  $CH_3OH$  with high selectivity. Similarly, a  $Co-Pi/\alpha-Fe_2O_3|BiFeO_3$  tandem PEC cell to regenerate NADH has been fabricated for the PEC  $CO_2$ -to- $CH_3OH$  conversion.<sup>[275]</sup> The NADH-dependent enzymes added into a separated cell containing the  $BiFeO_3$  photocathode permit the enzymatic reactions to be carried out at the optimal pH and avoid the poison effect from oxygenic reactions. However, the solar energy conversion efficiencies of these systems are limited by the low efficiency of PAs in the photocatalytic regeneration of coenzyme and also due to the nonideal catalytic environment for enzyme cascade since the optimal pH and temperature of each component in the enzyme cascade vary. The third type of the PA/enzyme hybrid uses living whole cells to ensure timely regeneration of coenzymes and to provide natural catalytic environments for all the members in the enzyme cascade,<sup>[276]</sup> which are coupled with PAs. In addition, after enzymes for biofuel production are broken down by environmental factors such as oxidative stress, they can be continuously renewed in the cells. In light of this, an integrated system was constructed through incubating acetogenic bacteria *Sporomusa ovata* within the photocathode (a SiNW array passivated by a 30 nm  $TiO_2$  protection layer) (Figure 13g), in which the SiNW array functions as a PA and the bacteria *S. ovata* reduces  $CO_2$  to acetic acid through an energy-efficient Wood–Ljungdahl pathway when it accepts electrons from the electrode.<sup>[265]</sup> Besides the merits mentioned in the above sections, inorganic nanoarray structures also provide more loading sites for enzyme immobilization and accelerate the diffusion of reactants, products, and cofactors in these abiotic–biotic photosynthetic hybrids.

Collectively, significant progress has been made to improve the catalytic kinetics and selectivity of PA/EC hybrid arrays for artificial photosynthesis. It can be concluded that the pitch of the PA arrays, CP matrix, the loading amount and species

**Figure 12.** a) Schematic illustration of the fabrication of the Ag/SiNWs photocathode. b) Size dependence of TOF for CO production on Ag NPs at various applied potentials. Reproduced with permission.<sup>[251]</sup> Copyright 2019, Royal Society of Chemistry. c)  $CH_4$  and d) CO production on as-grown GaN nanowires and Rh/Cr<sub>2</sub>O<sub>3</sub> decorated GaN nanowires as a function of illumination time. Reproduced with permission.<sup>[252]</sup> Copyright 2015, American Chemical Society. Side views of optimized configurations of  $CO_2$  adsorbed on the e) Pt(111) surface and f)  $Ti_3O_5H_6/Pt(111)$  surface. g) Differential charge density of  $CO_2$  adsorbed at the  $Ti_3O_5H_6/Pt(111)$  interface. Regions of yellow and blue indicate electronic charge gain and loss, respectively. Isosurface contours of electron density differences were drawn at  $\pm 0.002$  e Bohr<sup>-3</sup>. h) Faradaic efficiencies for CO at +0.27 V<sub>RHE</sub>. The FEs for CO of GaN/n<sup>+</sup>-p Si and  $TiO_2$ /GaN/n<sup>+</sup>-p Si photocathodes were measured at -0.33 V<sub>RHE</sub> due to the negligible photocurrent at an applied positive potential. The light illumination is ≈8 suns. Reproduced with permission.<sup>[253]</sup> Copyright 2018, American Chemical Society. i) Layer-by-layer molecular p-n-junction assembly formed by Zr(iv)-phosphonate bridging. The NPhN,  $Ru(CP)_2^{2+}$ , RuCt, and zirconium bridges are shown in green, yellow, red, and blue, respectively, in the integrated photocathode structure. j) n-GaN nanowires on the silicon substrate with the surface-immobilized molecular assemblies. k) Scanning electron microscope images (45° tilted) taken using MIRA3 (TESCAN) at an accelerating voltage of 10 kV for the pristine n-GaN nanowires grown on the substrate. l) Redox-potential diagram illustrating the relative energy levels (E), with red arrows showing the direction of photoinduced electron transfer. The two-photon excitation is illustrated by the “hv” notations, with  $Ru(CP)_2^{2+*}$  and Si\* representing the photon-excited chromophore and electrode. NPhN<sup>+/-0</sup>,  $Ru(CP)_2^{2+/-}$ , and  $Ru(CP)_2^{2+*/-}$  represent the one-electron reduction of the initial compounds with the potentials referenced to the NHE listed in the figure. The dashed arrow represents the transition from the excited state ( $Ru(CP)_2^{2+*}$ ) to the one-electron reduced chromophore ( $Ru(CP)_2^+$ ). Reproduced with permission.<sup>[254]</sup> Copyright 2019, Springer Nature.

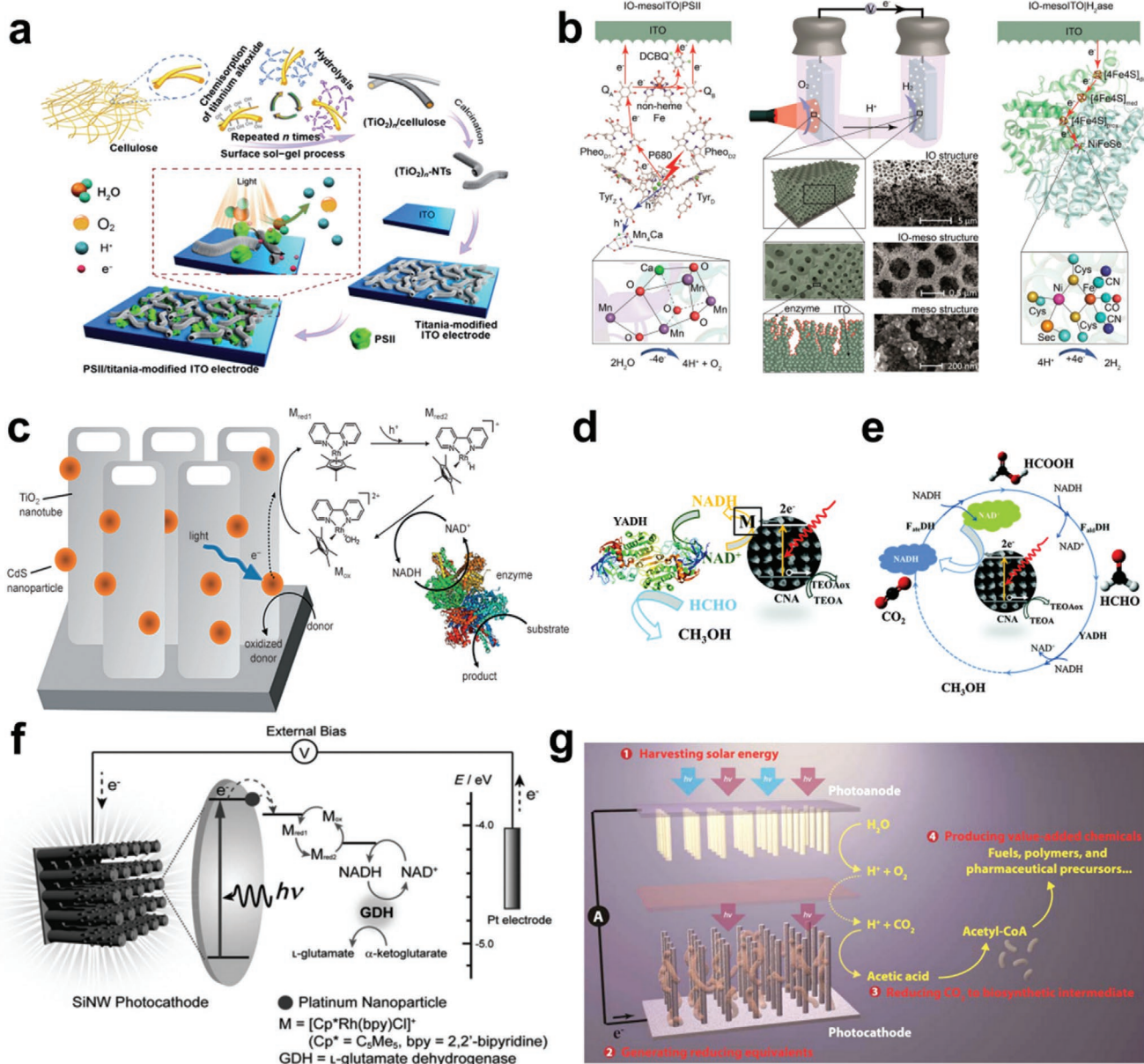


**Figure 13.** a) Schematic illustration of a fabrication process of a hybrid PSII/titania-modified ITO photoanode. Reproduced with permission.<sup>[260]</sup> Copyright 2016, Royal Society of Chemistry. b) Schematic representation of an enzymes/IO-mesoITO-based PEC cell. Water is photo-oxidized and  $\text{O}_2$  is generated by PSII on the IO-mesoITO (left), and aqueous protons are reduced by  $\text{H}_2\text{ase}$  on the IO-mesoITO (right). Reproduced with permission.<sup>[261]</sup> Copyright 2015, American Chemical Society. c) CdS quantum dot-sensitized  $\text{TiO}_2$  nanotube arrays for photocatalytic reduction of  $\text{NAD}^+$  allowing the operation of a coupled enzymatic system. Reproduced with permission.<sup>[262]</sup> Copyright 2011, Wiley-VCH GmbH. Schematic illustration of the conversion of d) formaldehyde or e)  $\text{CO}_2$  into  $\text{CH}_3\text{OH}$  by YADH or three consecutive enzymatic reactions, with  $\text{NADH}$  regenerated by CNA photocatalysis in the presence of a redox mediator. Reproduced with permission.<sup>[263]</sup> Copyright 2014, Royal Society of Chemistry. f) Schematic illustration of the visible-light-driven electroenzymatic reaction using a silicon nanowire (SiNW) photocathode. Photons absorbed by SiNWs generate excited electrons, which drift to the electrode/solution interface and reduce mediator (M). A chain of NADH regeneration occurs in the sequence of photoinduced electron transfer. Finally, the regenerated NADH is used to convert  $\alpha$ -ketoglutarate to L-glutamate using GDH. Reproduced with permission.<sup>[264]</sup> Copyright 2014, Wiley-VCH GmbH. g) Schematic of a general artificial photosynthetic approach. The proposed approach for solar-powered  $\text{CO}_2$  fixation includes four general components, which are responsible for: 1) harvesting solar energy, 2) generating reducing equivalents, 3) reducing  $\text{CO}_2$  to biosynthetic intermediates, and 4) producing value-added chemicals. This approach integrating materials science and biology combines the advantages of both solid-state devices and living organisms. Reproduced with permission.<sup>[265]</sup> Copyright 2015, American Chemical Society.

of ECs/enzymes, and the interaction between PA arrays and ECs/enzymes play key roles in regulating catalytic kinetics and selectivity. However, the exact nature of the catalytic

pathway and mechanism are still unclear; and the stability of the system is still a challenge, since the portion of the PA arrays that is not covered by ECs can easily get corroded in

**Table 1.** A comparison of photocurrent density, ABPE, IPCE, and stability among the given nanoarray examples for PEC water splitting.

Modulation strategy	Photoelectrode	Light source	Electrolyte	Photocurrent density	ABPE	IPCE	Stability [h]	Refs.
Light absorption	$\alpha\text{-Fe}_2\text{O}_3/\text{p-FTO}$	AM 1.5G	1 M NaOH	1.88 mA cm <sup>-2</sup> at 1.5 V <sub>RHE</sub>	N/A	65% at 300 nm	N/A	[110]
	ZnO/ZnFe <sub>2</sub> O <sub>4</sub>	AM 1.5G	0.1 M Na <sub>2</sub> SO <sub>4</sub>	1.41 mA cm <sup>-2</sup> at 1.23 V <sub>RHE</sub>	0.81% at 0.38 V <sub>RHE</sub>	45% at 365 nm	10	[136]
	TiO <sub>2</sub> with O vacancy	AM 1.5G	1 M NaOH	0.73 mA cm <sup>-2</sup> at 1.23 V <sub>RHE</sub>	1.31% at 0.40 V <sub>RHE</sub>	68% at 330 nm	1	[106]
Charge transport and transfer	g-CN	AM 1.5G	0.1 M Na <sub>2</sub> SO <sub>4</sub>	0.12 mA cm <sup>-2</sup> at 1.23 V <sub>RHE</sub>	N/A	15% at 360 nm	12	[57]
	Cu <sub>2</sub> O/TaON	AM 1.5G	0.5 M NaOH	3.06 mA cm <sup>-2</sup> at 1.00 V <sub>RHE</sub>	N/A	59% at 400 nm	1	[193]
	Au/TiO <sub>2</sub>	AM 1.5G	1 M KOH	2.32 mA cm <sup>-2</sup> at 1.00 V <sub>RHE</sub>	1.27% at 0.50 V <sub>RHE</sub>	N/A	5	[212]
Catalytic reaction	n <sup>+</sup> p-Si/SiO <sub>x</sub> /Ni/NiO <sub>x</sub> /NiFe-LDH	AM 1.5G	1 M KOH	≈37 mA cm <sup>-2</sup> at 1.23 V <sub>RHE</sub>	4.30% at 1.02 V <sub>RHE</sub>	N/A	68	[233]
	p <sup>+</sup> n-Si/SiO <sub>2</sub> /NiFe IO	AM 1.5G	1 M KOH	31.2 mA cm <sup>-2</sup> at 1.23 V <sub>RHE</sub>	N/A	N/A	11	[240]
	FeO <sub>x</sub> -CP/TiO <sub>2</sub>	AM 1.5G	0.5 M phosphate	1.60 mA cm <sup>-2</sup> at 1.23 V <sub>RHE</sub>	0.86% at 0.50 V <sub>RHE</sub>	68% at 420 nm	5	[246]

acidic or alkaline electrolytes. Therefore, more comprehensive and in-depth studies are needed for uncovering a clearer catalytic pathway and mechanism for designing and preparing nanoarrays with high stability and selectivity, with the assistance of a variety of theoretical tools and in situ analytical tools.

## 5. Conclusions and Outlooks

This review summarizes the recent development on diverse nanoarray structures with different functionalities that offer features such as increased light absorption, promoted charge transport and transfer, improved catalytic kinetics, as well as selectivity, which can pave a way for more rational designing of photoelectrodes for artificial photosynthesis. The following **Tables 1** and **2** summarize the specific performance parameters of some given nanoarray examples for PEC water splitting and CO<sub>2</sub>RR, respectively.

Despite many progresses, there is still plenty of room for further experimental and theoretical investigations of nanoarray structures to develop robust artificial photosynthetic systems for future high-performance solar energy conversion and storage. A few perspectives on the challenges existing in this field are listed below.

- 1) Taking full advantage of the solar spectrum to increase light absorption efficiency is challenging. Instead of single nanoarray structure/function design, integrating two or more different nanoarray structures with different mechanisms/materials for harvesting light into one system might further enhance light absorption intensity or extend light absorption range for solar energy conversion. At the same time, the manufacturing process of nanoarray structures for light absorption enhancement may have negative influence, such as introduction of various defects that act as charge recombination centers, disrupting charge transport and collection properties. Therefore, optimizing all light absorption strategies with least adverse effects is necessary to achieve maximum solar energy conversion performance.
- 2) Regarding charge transport, three points should be noted. First, the high specific surface area of nanoarray structures may lead to many surface defects, which are not beneficial for charge transport through the material/electrolyte interface. So, it is of great significance for the future design of nanoarrays to adopt effective methods to minimize the adverse effects of surface defects. Second, charge transport in nanoarray structures for artificial photosynthesis is usually controlled by diffusion, leading to high possibility of charge recombination due to the short charge diffusion length. Thus, changing

**Table 2.** A comparison of main product, yield, selectivity, and Faradic efficiency among the given nanoarray examples for PEC CO<sub>2</sub>RR.

Modulation strategy	Photoelectrode	Test condition	Test time [h]	Main product	Yield	Selectivity	Faradic efficiency [%]	Refs.
Light absorption	Au@CdS/IO-TiO <sub>2</sub>	100 mW cm <sup>-2</sup>	2	CH <sub>4</sub>	83.2 μmol g <sup>-1</sup>	98.6%	N/A	[74]
Charge transport and transfer	Cu <sub>2</sub> O-CuO	AM 1.5G, -0.2 V <sub>SCE</sub> , 0.1 M Na <sub>2</sub> SO <sub>4</sub>	1.5	CH <sub>3</sub> OH	≈85 μmol L <sup>-1</sup> cm <sup>-2</sup>	N/A	94–96	[203]
	CuFeO <sub>2</sub> /TNNTs	100 mW cm <sup>-2</sup> , -0.4 V <sub>SCE</sub> , 0.1 M NaHCO <sub>3</sub>	5	C <sub>2</sub> H <sub>5</sub> OH	3.3 μmol cm <sup>-2</sup>	N/A	75	[210]
Catalytic reaction	RA-Au/Si	100 mW cm <sup>-2</sup> , -0.03 V, 0.2 M KHCO <sub>3</sub>	N/A	CO	N/A	N/A	91	[239]
	Cu-Co <sub>3</sub> O <sub>4</sub>	10 mW cm <sup>-2</sup> , -0.9 V, 0.1 M Na <sub>2</sub> SO <sub>4</sub>	8	HCOO <sup>-</sup>	6.75 mmol L <sup>-1</sup> cm <sup>-2</sup>	≈100%	N/A	[258]
	ZIF9-Co <sub>3</sub> O <sub>4</sub>	AM 1.5G, -0.9 V, 0.1 M Na <sub>2</sub> SO <sub>4</sub>	8	HCOO <sup>-</sup>	578.7 μmol L <sup>-1</sup> cm <sup>-2</sup>	≈99%	70.5	[259]
	Ag/SiNWs	AM 1.5G, -1.2 V <sub>RHE</sub> , 0.1 M KHCO <sub>3</sub>	4	CO	348 μmol L <sup>-1</sup> cm <sup>-2</sup>	N/A	70	[251]

the transport process from diffusion- to drift-controlled will greatly shorten the charge transport time and improve the collection efficiency. In long term, designing new materials or new heterostructures to optimize the built-in electric field strength or SCR, might be an important research direction. Third, although non-noble metals have been used to replace noble metals for low-cost SC-M heterojunctions, effective solar energy conversion is still limited by their instability. Hence, the stable non-noble metal counterparts need to be developed for smooth interfacial charge transport.

- 3) In terms of the use of abiotic- and biotic-ECs to construct PA/EC hybrid nanoarrays, the stability and catalytic efficiency of the designed structure need to be further improved. Abiotic hybrid systems display a good catalytic stability owing to their inherent structural stability. However, they also have weaknesses such as low catalytic selectivity, which might be due to the lack of the suitable catalytic microenvironment and small difference among the energy levels of different catalytic products.<sup>[277,278]</sup> By introducing the biotic enzymes or cells with superior catalytic microenvironment and the specific catalytic pathway to construct abiotic-biotic hybrid systems can significantly increase catalytic selectivity. Nevertheless, many issues should also be addressed in abiotic-biotic hybrid systems. For instance, considering the unclear mechanism of the charge transfer at the abiotic-biotic interface, it is very difficult to match the electron flux of abiotic components and the turnover frequency of biotic parts for achieving high catalytic efficiency. In addition, the long-term stability of the abiotic-biotic hybrid system, which can be affected by the deactivation of the biotic enzymes or cells by the oxidation stress, etc., need to be improved.<sup>[279]</sup>

Thus, the future study should focus on improving stability by employing more stable ECs and surface passivation layer without sacrificing the activity, as well as exploring new mechanisms such as self-repairing/healing. For the PA/biotic-EC hybrids, the great challenge lies in how to make PA and biotic systems compatible and communicable, such as how to improve photosensitizing ability of PAs at the same time limiting photo-oxidative damage to enzymes or living cells; how to balance the solution environment that maintains the long-time photo-stability of PAs and provides the optimal catalytic environment for enzymes. Therefore, enhancing the environmental stress tolerance of enzymes by engineering enzymes and creating conditions that mimic their natural local environment either by changing the reaction medium or by surface modification of PAs are the prerequisite for obtaining a long-term stability and high efficiency in these systems. Meanwhile, the immobilization methods, which will affect both the stability of the hybrid (avoiding the enzymes/whole cells falling off from the PA's surface) and the interfacial charge transfer between PAs and enzymes/whole cells, should also be optimized. In addition, the undesired side reactions or metabolism pathways that inhibit cofactor regeneration or consume the photogenerated electrons for production of fuels or chemicals is another limitation factor. Therefore, simplifying the electron transfer chain to avoid the undesired side reactions or metabolism pathways (optimizing metabolic networks through synthetic biology) will be helpful

to achieve highly efficient artificial photosynthesis. Apart from the above-mentioned optimization through modulation of the enzyme/whole cell and the PA/enzyme interface, a more rational design of PA nanoarray structures is also required to improve solar energy conversion efficiency. For example, the IO with the hierarchical pore architecture will ensure the macromolecular biological catalysts (enzymes) fitted in the large pores with suitable sizes, and the small-molecular reactants and products transported in and out through the adjacent small pores. Thus, each enzymatic reaction can take place in a local environment and also well communicate with each other, leading to a high efficiency of the multienzymatic cascade reactions. Meanwhile, the concentration and stability of the enzyme loaded in this structure are greatly increased as compared with that immobilized on the planer structure, which are also essential for high catalytic efficiency.

- 4) Advanced technologies need to be developed for large-scale production and precise characterization of nanoarray structures. First, conventional techniques for preparation of nanoarray structures usually involve technologically demanding and tedious processes with high cost, which limit the application. Therefore, exploring facile and low-cost methods to realize easy and tunable fabrication of nanoarray structures is crucial in the future research. Second, real-time and *in situ* characterizations to gain the important information of the nanoarray structural evolution, composition, and interface change during artificial photosynthesis are critical. Over the past decades, the advance of *in situ* characterization techniques, such as transient absorption spectroscopy, *in situ* infrared spectroscopy, as well as X-ray spectroscopy techniques, have become a powerful tool for mechanistic studies on energy conversion. More important, a combination of different *in situ* characterization techniques is critical to understand the full picture of reaction mechanism and the photoelectrode materials' structural change during solar energy conversion. The findings will provide important information for future structure design and surface engineering of nanoarrays.
- 5) Besides experimentally constructing nanoarray structures in photosynthetic systems, designing new nanoarray structure models with different parameters (such as composition, morphology, and arrangement) through computational simulations is also important. It can not only provide an in-depth understanding of the specific advantages and mechanisms of light absorption, charge transport and transfer, and catalytic reaction in artificial photosynthesis, but also save the time and cost for optimizing the structural parameters in the experiments. It is well-known that artificial photosynthesis is a multistep process, and the overall device performance is associated with the efficiency of each step/component. Thus, synergistic effects of the various subprocesses/components is central for effective solar energy conversion of fuels and chemicals.

In a word, this review focuses on the three key aspects, namely, light absorption, charge transport and transfer, catalytic kinetics and selectivity, and their related regulation strategies

involved in artificial photosynthesis for nanoarray structures. Furthermore, a few perspectives on the challenges to further improve solar energy conversion efficiencies are provided. The basic principles summarized in this review may offer helpful guidance and reference to the future rational design and construction of nanoarray structures for artificial photosynthesis of renewable fuels and high value-added chemicals. With ongoing progress of science and technologies, we believe that nanoarray structures will play highly beneficial roles in artificial photosynthesis.

## Acknowledgements

L.T., Q.X., and C.Z. contributed equally to this work. The authors acknowledge financial support for this work from the Strategic Priority Research Program of CAS (XDB36000000), the National Natural Science Foundation of China (21422303, 21573049, 21872043, 81602643, and 22002028), the National Basic Research Plan of China (2016YFA0201600), the Beijing Natural Science Foundation (2142036), and the Knowledge Innovation Program, Youth Innovation Promotion Association, and Special Program of "One Belt One Road" of CAS. The authors also thank Yawen Dai for the help with the homojunction part, and Wenjing Xie and Rajender Boddula for proofreading.

## Conflict of Interest

The authors declare no conflict of interest.

## Keywords

artificial photosynthesis, charge transport and transfer, light absorption, nanoarray structure, solar energy conversion

Received: October 20, 2020

Revised: January 25, 2021

Published online:

- [1] B. A. Pinaud, J. D. Benck, L. C. Seitz, A. J. Forman, Z. Chen, T. G. Deutsch, B. D. James, K. N. Baum, G. N. Baum, S. Ardo, H. Wang, E. Miller, T. F. Jaramillo, *Energy Environ. Sci.* **2013**, *6*, 1983.
- [2] G. Xie, K. Zhang, B. Guo, Q. Liu, L. Fang, J. R. Gong, *Adv. Mater.* **2013**, *25*, 3820.
- [3] T. Bak, J. Nowotny, M. Rekas, C. C. Sorrell, *Int. J. Hydrogen Energy* **2002**, *27*, 991.
- [4] Q. Zhou, Z. Fang, J. Li, M. Wang, *Microporous Mesoporous Mater.* **2015**, *202*, 22.
- [5] S. Hoang, P.-X. Gao, *Adv. Energy Mater.* **2016**, *6*, 1600683.
- [6] C. Jiang, S. J. A. Moniz, A. Wang, T. Zhang, J. Tang, *Chem. Soc. Rev.* **2017**, *46*, 4645.
- [7] M. G. Walter, E. L. Warren, J. R. McKone, S. W. Boettcher, Q. Mi, E. A. Santori, N. S. Lewis, *Chem. Rev.* **2010**, *110*, 6446.
- [8] J. R. McKone, N. S. Lewis, H. B. Gray, *Chem. Mater.* **2014**, *26*, 407.
- [9] M. Graetzel, *Acc. Chem. Res.* **1981**, *14*, 376.
- [10] Y. Tachibana, L. Vayssieres, J. R. Durrant, *Nat. Photonics* **2012**, *6*, 511.
- [11] S. Ye, R. Wang, M.-Z. Wu, Y.-P. Yuan, *Appl. Surf. Sci.* **2015**, *358*, 15.
- [12] J. K. Stolarczyk, S. Bhattacharyya, L. Polavarapu, J. Feldmann, *ACS Catal.* **2018**, *8*, 3602.
- [13] G. Centi, S. Perathoner, *ChemSusChem* **2010**, *3*, 195.
- [14] T. Hisatomi, K. Domon, *Faraday Discuss.* **2017**, *198*, 11.
- [15] M. Ali, F. Zhou, K. Chen, C. Kotzur, C. Xiao, L. Bourgeois, X. Zhang, D. R. MacFarlane, *Nat. Commun.* **2016**, *7*, 11335.
- [16] R. Lan, S. Tao, *Front. Energy Res.* **2014**, *2*, 35.
- [17] L. Zhang, Z.-J. Zhao, T. Wang, J. Gong, *Chem. Soc. Rev.* **2018**, *47*, 5423.
- [18] D. Zhang, M. Yang, *Phys. Chem. Chem. Phys.* **2013**, *15*, 18523.
- [19] R. van de Krol, Y. Liang, J. Schoonman, *J. Mater. Chem.* **2008**, *18*, 2311.
- [20] J. Li, N. Wu, *Catal. Sci. Technol.* **2015**, *5*, 1360.
- [21] C. Liu, N. P. Dasgupta, P. Yang, *Chem. Mater.* **2014**, *26*, 415.
- [22] X. Li, J. Wen, J. Low, Y. Fang, J. Yu, *Sci. China Mater.* **2014**, *57*, 70.
- [23] R. Li, *Chin. J. Catal.* **2018**, *39*, 1180.
- [24] A. Kudo, Y. Miseki, *Chem. Soc. Rev.* **2009**, *38*, 253.
- [25] S. J. A. Moniz, S. A. Shevlin, D. J. Martin, Z.-X. Guo, J. Tang, *Energy Environ. Sci.* **2015**, *8*, 731.
- [26] A. G. Tamirat, J. Rick, A. A. Dubale, W.-N. Su, B.-J. Hwang, *Nanoscale Horiz.* **2016**, *1*, 243.
- [27] Z. Li, J. Feng, S. Yan, Z. Zou, *Nano Today* **2015**, *10*, 468.
- [28] P. M. Rao, L. Cai, C. Liu, I. S. Cho, C. H. Lee, J. M. Weisse, P. Yang, X. Zheng, *Nano Lett.* **2014**, *14*, 1099.
- [29] G. D. Scholes, G. Rumbles, *Nat. Mater.* **2006**, *5*, 683.
- [30] N. C. Giebink, G. P. Wiederrecht, M. R. Wasielewski, S. R. Forrest, *Phys. Rev. B* **2011**, *83*, 195326.
- [31] R. J. Holmes, S. Kéna-Cohen, V. M. Menon, S. R. Forrest, *Phys. Rev. B* **2006**, *74*, 235211.
- [32] A. I. Hochbaum, P. Yang, *Chem. Rev.* **2010**, *110*, 527.
- [33] H. Wang, X. Zhang, Y. Xie, *Mater. Today* **2019**, *23*, 72.
- [34] K. Feron, J. W. Belcher, J. C. Fell, C. P. Dastoor, *Int. J. Mol. Sci.* **2012**, *13*, 17019.
- [35] F. E. Osterloh, *Chem. Soc. Rev.* **2013**, *42*, 2294.
- [36] C. Li, A. Li, Z. Luo, J. Zhang, X. Chang, Z. Huang, T. Wang, J. Gong, *Angew. Chem., Int. Ed.* **2017**, *56*, 4150.
- [37] Z. Zhang, J. T. Yates, *Chem. Rev.* **2012**, *112*, 5520.
- [38] Y. Qiu, Z. Pan, H. Chen, D. Ye, L. Guo, Z. Fan, S. Yang, *Sci. Bull.* **2019**, *64*, 1348.
- [39] V. Kumaravel, J. Bartlett, S. C. Pillai, *ACS Energy Lett.* **2020**, *5*, 486.
- [40] L. Steier, I. Herraiz-Cardona, S. Gimenez, F. Fabregat-Santiago, J. Bisquert, S. D. Tilley, M. Grätzel, *Adv. Funct. Mater.* **2014**, *24*, 7681.
- [41] E. Samuel, B. Joshi, M.-W. Kim, M. T. Swihart, S. S. Yoon, *Nano Energy* **2020**, *72*, 104648.
- [42] W. Yang, R. R. Prabhakar, J. Tan, S. D. Tilley, J. Moon, *Chem. Soc. Rev.* **2019**, *48*, 4979.
- [43] Y. Lin, G. Yuan, R. Liu, S. Zhou, S. W. Sheehan, D. Wang, *Chem. Phys. Lett.* **2011**, *507*, 209.
- [44] J. Su, L. Guo, N. Bao, C. A. Grimes, *Nano Lett.* **2011**, *11*, 1928.
- [45] H. Zhang, Q. Ding, D. He, H. Liu, W. Liu, Z. Li, B. Yang, X. Zhang, L. Lei, S. Jin, *Energy Environ. Sci.* **2016**, *9*, 3113.
- [46] Y. Yu, Z. Zhang, X. Yin, A. Kvitt, Q. Liao, Z. Kang, X. Yan, Y. Zhang, X. Wang, *Nat. Energy* **2017**, *2*, 17045.
- [47] M. Zhou, Y. Xu, Y. Lei, *Nano Today* **2018**, *20*, 33.
- [48] H. Zhao, M. Zhou, L. Wen, Y. Lei, *Nano Energy* **2015**, *13*, 790.
- [49] W. Wang, L. Qi, *Adv. Funct. Mater.* **2019**, *29*, 1807275.
- [50] J. Liu, S.-M. Xu, Y. Li, R. Zhang, M. Shao, *Appl. Catal., B* **2020**, *264*, 118540.
- [51] V. J. Babu, S. Vempati, T. Uyar, S. Ramakrishna, *Phys. Chem. Chem. Phys.* **2015**, *17*, 2960.
- [52] B. Yao, J. Zhang, X. Fan, J. He, Y. Li, *Small* **2019**, *15*, 1803746.
- [53] Y. Hou, T. Li, S. Yan, Z. Zou, *Appl. Catal., B* **2020**, *269*, 118777.
- [54] C. Zhen, L. Wang, G. Liu, G. Q. Lu, H.-M. Cheng, *Chem. Commun.* **2013**, *49*, 3019.
- [55] S. Liu, C. Han, Z.-R. Tang, Y.-J. Xu, *Mater. Horiz.* **2016**, *3*, 270.

- [56] W. Tian, C. Chen, L. Meng, W. Xu, F. Cao, L. Li, *Adv. Energy Mater.* **2020**, *10*, 1903951.
- [57] B. Guo, L. Tian, W. Xie, A. Batool, G. Xie, Q. Xiang, S. U. Jan, R. Boddula, J. R. Gong, *Nano Lett.* **2018**, *18*, 5954.
- [58] Y. Tak, S. J. Hong, J. S. Lee, K. Yong, *J. Mater. Chem.* **2009**, *19*, 5945.
- [59] X. Yang, A. Wolcott, G. Wang, A. Sobo, R. C. Fitzmorris, F. Qian, J. Z. Zhang, Y. Li, *Nano Lett.* **2009**, *9*, 2331.
- [60] A. Wolcott, W. A. Smith, T. R. Kuykendall, Y. Zhao, J. Z. Zhang, *Small* **2009**, *5*, 104.
- [61] F. Ning, M. Shao, S. Xu, Y. Fu, R. Zhang, M. Wei, D. G. Evans, X. Duan, *Energy Environ. Sci.* **2016**, *9*, 2633.
- [62] J. Zheng, Y. Lyu, M. Qiao, R. Wang, Y. Zhou, H. Li, C. Chen, Y. Li, H. Zhou, S. P. Jiang, S. Wang, *Chem* **2019**, *5*, 617.
- [63] W.-T. Sun, Y. Yu, H.-Y. Pan, X.-F. Gao, Q. Chen, L.-M. Peng, *J. Am. Chem. Soc.* **2008**, *130*, 1124.
- [64] X.-F. Gao, H.-B. Li, W.-T. Sun, Q. Chen, F.-Q. Tang, L.-M. Peng, *J. Phys. Chem. C* **2009**, *113*, 7531.
- [65] Z.-Q. Wei, X.-C. Dai, S. Hou, Y.-B. Li, M.-H. Huang, T. Li, S. Xu, F.-X. Xiao, *J. Mater. Chem. A* **2020**, *8*, 177.
- [66] D. Hu, P. Diao, D. Xu, M. Xia, Y. Gu, Q. Wu, C. Li, S. Yang, *Nanoscale* **2016**, *8*, 5892.
- [67] W. Li, P. Da, Y. Zhang, Y. Wang, X. Lin, X. Gong, G. Zheng, *ACS Nano* **2014**, *8*, 11770.
- [68] J. Wang, C. Liu, Y. Liu, S. Chen, *CrystEngComm* **2020**, *22*, 1914.
- [69] J. Liu, Y. Y. Cai, Z. F. Tian, G. S. Ruan, Y. X. Ye, C. H. Liang, G. S. Shao, *Nano Energy* **2014**, *9*, 282.
- [70] Y. Li, X. Wei, X. Yan, J. Cai, A. Zhou, M. Yang, K. Liu, *Phys. Chem. Chem. Phys.* **2016**, *18*, 10255.
- [71] M. Li, X. Tu, Y. Su, J. Lu, J. Hu, B. Cai, Z. Zhou, Z. Yang, Y. Zhang, *Nanoscale* **2018**, *10*, 1153.
- [72] M. Zhou, J. Bao, Y. Xu, J. Zhang, J. Xie, M. Guan, C. Wang, L. Wen, Y. Lei, Y. Xie, *ACS Nano* **2014**, *8*, 7088.
- [73] C. Cheng, S. K. Karuturi, L. Liu, J. Liu, H. Li, L. T. Su, A. I. Y. Tok, H. J. Fan, *Small* **2012**, *8*, 37.
- [74] Y. Wei, J. Jiao, Z. Zhao, J. Liu, J. Li, G. Jiang, Y. Wang, A. Duan, *Appl. Catal., B* **2015**, *179*, 422.
- [75] Y. Zhou, L. Zhang, L. Lin, B. R. Wygant, Y. Liu, Y. Zhu, Y. Zheng, C. B. Mullins, Y. Zhao, X. Zhang, G. Yu, *Nano Lett.* **2017**, *17*, 8012.
- [76] J. Li, Z. Liu, Z. Zhu, *Appl. Surf. Sci.* **2014**, *320*, 146.
- [77] Y. Hou, F. Zuo, A. Dagg, P. Feng, *Angew. Chem., Int. Ed.* **2013**, *52*, 1248.
- [78] Y. Hou, F. Zuo, A. P. Dagg, J. Liu, P. Feng, *Adv. Mater.* **2014**, *26*, 5043.
- [79] Y. Zhong, S. Yang, S. Zhang, X. Cai, Q. Gao, X. Yu, Y. Xu, X. Zhou, F. Peng, Y. Fang, *J. Power Sources* **2019**, *430*, 32.
- [80] T. Mahvelati-Shamsabadi, B.-K. Lee, *Catal. Today* **2020**, *358*, 412.
- [81] S. Tang, W. Qiu, S. Xiao, Y. Tong, S. Yang, *Energy Environ. Sci.* **2020**, *13*, 660.
- [82] X. Sheng, T. Xu, X. Feng, *Adv. Mater.* **2019**, *31*, 1805132.
- [83] W.-Q. Wu, Y.-F. Xu, J.-F. Liao, L. Wang, D.-B. Kuang, *Nano Energy* **2019**, *62*, 791.
- [84] Š. Kment, K. Sivula, A. Naldoni, S. P. Sarmah, H. Kmentová, M. Kulkarni, Y. Rambabu, P. Schmuki, R. Zbořil, *Prog. Mater. Sci.* **2020**, *110*, 100632.
- [85] A. B. Murphy, P. R. F. Barnes, L. K. Randeniya, I. C. Plumb, I. E. Grey, M. D. Horne, J. A. Glasscock, *Int. J. Hydrogen Energy* **2006**, *31*, 1999.
- [86] H. Dotan, K. Sivula, M. Grätzel, A. Rothschild, S. C. Warren, *Energy Environ. Sci.* **2011**, *4*, 958.
- [87] W. Wang, J. Dong, X. Ye, Y. Li, Y. Ma, L. Qi, *Small* **2016**, *12*, 1469.
- [88] L. Zhang, D. Bahnemann, *ChemSusChem* **2013**, *6*, 283.
- [89] Y. Hu, X. Yan, Y. Gu, X. Chen, Z. Bai, Z. Kang, F. Long, Y. Zhang, *Appl. Surf. Sci.* **2015**, *339*, 122.
- [90] Z. Wang, T. D. Nguyen, L. P. Yeo, C. K. Tan, L. Gan, A. I. Y. Tok, *Small* **2020**, *16*, 1905826.
- [91] K. X. Wang, Z. Yu, V. Liu, Y. Cui, S. Fan, *Nano Lett.* **2012**, *12*, 1616.
- [92] J.-Y. Jung, M. J. Choi, K. Zhou, X. Li, S.-W. Jee, H.-D. Um, M.-J. Park, K.-T. Park, J. H. Bang, J.-H. Lee, *J. Mater. Chem. A* **2014**, *2*, 833.
- [93] L. Gao, Y. Cui, R. H. J. Vervuurt, D. van Dam, R. P. J. van Veldhoven, J. P. Hofmann, A. A. Bol, J. E. M. Haverkort, P. H. L. Notten, E. P. A. M. Bakkers, E. J. M. Hensen, *Adv. Funct. Mater.* **2016**, *26*, 679.
- [94] S. Xu, F. Jiang, F. Gao, L. Wang, J. Teng, D. Fu, H. Zhang, W. Yang, S. Chen, *ACS Appl. Mater. Interfaces* **2020**, *12*, 20469.
- [95] G. L. Chiarello, A. Zuliani, D. Ceresoli, R. Martinazzo, E. Sellì, *ACS Catal.* **2016**, *6*, 1345.
- [96] X. Chen, J. Ye, S. Ouyang, T. Kako, Z. Li, Z. Zou, *ACS Nano* **2011**, *5*, 4310.
- [97] J. Luo, J. Chen, H. Wang, H. Liu, *J. Power Sources* **2016**, *303*, 287.
- [98] X. Zhang, Y. Liu, Z. Kang, *ACS Appl. Mater. Interfaces* **2014**, *6*, 4480.
- [99] J. Lee, S. Mubeen, X. Ji, G. D. Stucky, M. Moskovits, *Nano Lett.* **2012**, *12*, 5014.
- [100] Y. Abbas, Z. Zuhra, N. Akhtar, S. Ali, J. R. Gong, *ACS Appl. Energy Mater.* **2018**, *1*, 3529.
- [101] X. Xu, Z. Bao, W. Tang, H. Wu, J. Pan, J. Hu, H. Zeng, *Carbon* **2017**, *121*, 201.
- [102] K.-H. Ye, Z. Wang, J. Gu, S. Xiao, Y. Yuan, Y. Zhu, Y. Zhang, W. Mai, S. Yang, *Energy Environ. Sci.* **2017**, *10*, 772.
- [103] L. Zhang, P. Cui, H. Yang, J. Chen, F. Xiao, Y. Guo, Y. Liu, W. Zhang, F. Huo, B. Liu, *Adv. Sci.* **2016**, *3*, 1500243.
- [104] S. K. Srivastava, D. Kumar, P. K. Singh, M. Kar, V. Kumar, M. Husain, *Sol. Energy Mater. Sol. Cells* **2010**, *94*, 1506.
- [105] J. Li, S. K. Cushing, P. Zheng, F. Meng, D. Chu, N. Wu, *Nat. Commun.* **2013**, *4*, 2651.
- [106] Q. Kang, J. Cao, Y. Zhang, L. Liu, H. Xu, J. Ye, *J. Mater. Chem. A* **2013**, *1*, 5766.
- [107] X. Zhang, F. Wang, H. Huang, H. Li, X. Han, Y. Liu, Z. Kang, *Nanoscale* **2013**, *5*, 2274.
- [108] B. Chen, Z. Zhang, M. Baek, S. Kim, W. Kim, K. Yong, *Appl. Catal., B* **2018**, *237*, 763.
- [109] G. Kang, J. Yoo, J. Ahn, K. Kim, *Nano Today* **2015**, *10*, 22.
- [110] K. Kim, I.-H. Kim, K.-Y. Yoon, J. Lee, J.-H. Jang, *J. Mater. Chem. A* **2015**, *3*, 7706.
- [111] Y. Mi, L. Wen, R. Xu, Z. Wang, D. Cao, Y. Fang, Y. Lei, *Adv. Energy Mater.* **2016**, *6*, 1501496.
- [112] D. Bialusiewski, J. S. Hoppius, R. Froehnoven, M. Deo, Y. Gönüllü, T. Fischer, E. L. Gurevich, S. Mathur, *Adv. Eng. Mater.* **2018**, *20*, 1800167.
- [113] M. Seol, H. Kim, W. Kim, K. Yong, *Electrochim. Commun.* **2010**, *12*, 1416.
- [114] C. W. Lai, S. Sreekanth, *Int. J. Hydrogen Energy* **2013**, *38*, 2156.
- [115] C. Cheng, H. Zhang, W. Ren, W. Dong, Y. Sun, *Nano Energy* **2013**, *2*, 779.
- [116] H. N. Hieu, N. Q. Dung, J. Kim, D. Kim, *Nanoscale* **2013**, *5*, 5530.
- [117] V. K. Narasimhan, Y. Cui, *Nanophotonics* **2013**, *2*, 187.
- [118] K.-H. Tsui, Q. Lin, H. Chou, Q. Zhang, H. Fu, P. Qi, Z. Fan, *Adv. Mater.* **2014**, *26*, 2805.
- [119] J. Zhu, Z. Yu, G. F. Burkhardt, C.-M. Hsu, S. T. Connor, Y. Xu, Q. Wang, M. McGehee, S. Fan, Y. Cui, *Nano Lett.* **2009**, *9*, 279.
- [120] H. Sai, H. Fujii, K. Arafune, Y. Ohshita, M. Yamaguchi, Y. Kanamori, H. Yugami, *Appl. Phys. Lett.* **2006**, *88*, 201116.
- [121] S. Lou, X. Guo, T. Fan, D. Zhang, *Energy Environ. Sci.* **2012**, *5*, 9195.
- [122] K. Peng, Y. Xu, Y. Wu, Y. Yan, S.-T. Lee, J. Zhu, *Small* **2005**, *1*, 1062.
- [123] J. Y. Chen, K. W. Sun, *Sol. Energy Mater. Sol. Cells* **2010**, *94*, 629.
- [124] J. Oh, T. G. Deutsch, H.-C. Yuan, H. M. Branz, *Energy Environ. Sci.* **2011**, *4*, 1690.
- [125] T. Wang, J. Gong, *Angew. Chem., Int. Ed.* **2015**, *54*, 10718.

- [126] Y.-F. Huang, S. Chattopadhyay, Y.-J. Jen, C.-Y. Peng, T.-A. Liu, Y.-K. Hsu, C.-L. Pan, H.-C. Lo, C.-H. Hsu, Y.-H. Chang, C.-S. Lee, K.-H. Chen, L.-C. Chen, *Nat. Nanotechnol.* **2007**, 2, 770.
- [127] S. Nishimura, N. Abrams, B. A. Lewis, L. I. Halaoui, T. E. Mallouk, K. D. Benkstein, J. van de Lagemaat, A. J. Frank, *J. Am. Chem. Soc.* **2003**, 125, 6306.
- [128] H. Zhao, Z. Hu, J. Liu, Y. Li, M. Wu, G. Van Tendeloo, B.-L. Su, *Nano Energy* **2018**, 47, 266.
- [129] X. Zheng, Y. Yang, S. Chen, L. Zhang, *Chin. J. Catal.* **2018**, 39, 379.
- [130] R. W. Boyd, D. J. Gauthier, *Science* **2009**, 326, 1074.
- [131] T. Baba, *Nat. Photonics* **2008**, 2, 465.
- [132] Z. Zhang, X. Yang, M. N. Hedhili, E. Ahmed, L. Shi, P. Wang, *ACS Appl. Mater. Interfaces* **2014**, 6, 691.
- [133] A. Mihi, H. Míguez, *J. Phys. Chem. B* **2005**, 109, 15968.
- [134] H. Zhang, W. Zhou, Y. Yang, C. Cheng, *Small* **2017**, 13, 1603840.
- [135] C. Li, X. Zhu, H. Zhang, Z. Zhu, B. Liu, C. Cheng, *Adv. Mater. Interfaces* **2015**, 2, 1500428.
- [136] T. Yang, J. Xue, H. Tan, A. Xie, S. Li, W. Yan, Y. Shen, *J. Mater. Chem. A* **2018**, 6, 1210.
- [137] J. Jiao, Y. Wei, Z. Zhao, J. Liu, J. Li, A. Duan, G. Jiang, *Ind. Eng. Chem. Res.* **2014**, 53, 17345.
- [138] S. Linic, P. Christopher, D. B. Ingram, *Nat. Mater.* **2011**, 10, 911.
- [139] D. O. Sigle, L. Zhang, S. Ithurria, B. Dubertret, J. J. Baumberg, *J. Phys. Chem. Lett.* **2015**, 6, 1099.
- [140] S. K. Gray, *J. Phys. Chem. C* **2013**, 117, 1983.
- [141] M. Rycenga, C. M. Cobley, J. Zeng, W. Li, C. H. Moran, Q. Zhang, D. Qin, Y. Xia, *Chem. Rev.* **2011**, 111, 3669.
- [142] S. K. Cushing, N. Wu, *Electrochem. Soc. Interface* **2013**, 22, 63.
- [143] S. Ramadurgam, T.-G. Lin, C. Yang, *Nano Lett.* **2014**, 14, 4517.
- [144] P. Peerakittikhajohn, T. Butburee, J.-H. Yun, H. Chen, R. M. Richards, L. Wang, *J. Mater. Chem. A* **2015**, 3, 20127.
- [145] H. Gao, C. Liu, H. E. Jeong, P. Yang, *ACS Nano* **2012**, 6, 234.
- [146] Z. Li, L. Shi, D. Franklin, S. Koul, A. Kushima, Y. Yang, *Nano Energy* **2018**, 51, 400.
- [147] H. Li, X. Li, W. Dong, J. Xi, G. Du, Z. Ji, *J. Alloys Compd.* **2018**, 768, 830.
- [148] Z. Liu, J. Wu, J. Zhang, *Int. J. Hydrogen Energy* **2016**, 41, 20529.
- [149] C. Rhodes, S. Franzen, J.-P. Maria, M. Losego, D. N. Leonard, B. Laughlin, G. Duscher, S. Weibel, *J. Appl. Phys.* **2006**, 100, 054905.
- [150] L. Mascaretti, A. Dutta, Š. Kment, V. M. Shalaev, A. Boltasseva, R. Zbořil, A. Naldoni, *Adv. Mater.* **2019**, 31, 1805513.
- [151] J. Li, S. K. Cushing, P. Zheng, T. Senty, F. Meng, A. D. Bristow, A. Manivannan, N. Wu, *J. Am. Chem. Soc.* **2014**, 136, 8438.
- [152] C. Duan, H. Wang, X. Ou, F. Li, X. Zhang, *ACS Appl. Mater. Interfaces* **2014**, 6, 9742.
- [153] Y. Sun, B. Xu, Q. Shen, L. Hang, D. Men, T. Zhang, H. Li, C. Li, Y. Li, *ACS Appl. Mater. Interfaces* **2017**, 9, 31897.
- [154] Z. Zhang, L. Zhang, M. N. Hedhili, H. Zhang, P. Wang, *Nano Lett.* **2012**, 13, 14.
- [155] G. Wang, Y. Ling, Y. Li, *Nanoscale* **2012**, 4, 6682.
- [156] M. Shang, H. Hu, G. Lu, Y. Bi, *J. Mater. Chem. A* **2016**, 4, 5849.
- [157] L. Cai, F. Ren, M. Wang, G. Cai, Y. Chen, Y. Liu, S. Shen, L. Guo, *Int. J. Hydrogen Energy* **2015**, 40, 1394.
- [158] X. Chen, S. Shen, L. Guo, S. S. Mao, *Chem. Rev.* **2010**, 110, 6503.
- [159] Q. Li, H. Meng, P. Zhou, Y. Zheng, J. Wang, J. Yu, J. R. Gong, *ACS Catal.* **2013**, 3, 882.
- [160] J. H. Park, S. Kim, A. J. Bard, *Nano Lett.* **2006**, 6, 24.
- [161] M. N. Huda, Y. Yan, S.-H. Wei, M. M. Al-Jassim, *Phys. Rev. B* **2008**, 78, 195204.
- [162] H. Li, J. Chen, Z. Xia, J. Xing, *J. Mater. Chem. A* **2015**, 3, 699.
- [163] J. Zhang, K. Tse, M. Wong, Y. Zhang, J. Zhu, *Front. Phys.* **2016**, 11, 117405.
- [164] H. M. Chen, C. K. Chen, R.-S. Liu, C.-C. Wu, W.-S. Chang, K.-H. Chen, T.-S. Chan, J.-F. Lee, D. P. Tsai, *Adv. Energy Mater.* **2011**, 1, 742.
- [165] R. Wang, X. Xu, Y. Zhang, Z. Chang, Z. Sun, W.-F. Dong, *Nanoscale* **2015**, 7, 11082.
- [166] J. Li, B. Liu, A. Wu, B. Yang, W. Yang, F. Liu, X. Zhang, V. An, X. Jiang, *Inorg. Chem.* **2018**, 57, 5240.
- [167] Q. Liu, B. Guo, Z. Rao, B. Zhang, J. R. Gong, *Nano Lett.* **2013**, 13, 2436.
- [168] Q. Xin, Q. Liu, L. Geng, Q. Fang, J. R. Gong, *Adv. Healthcare Mater.* **2017**, 6, 1601011.
- [169] J. Sun, Q. Xin, Y. Yang, H. Shah, H. Cao, Y. Qi, J. R. Gong, J. Li, *Chem. Commun.* **2018**, 54, 715.
- [170] Y. Zhao, Q. Liu, S. Shakoor, J. R. Gong, D. Wang, *Toxicol. Res.* **2015**, 4, 270.
- [171] Q. Xin, H. Shah, A. Nawaz, W. Xie, M. Z. Akram, A. Batool, L. Tian, S. U. Jan, R. Boddula, B. Guo, Q. Liu, J. R. Gong, *Adv. Mater.* **2018**, 31, 1804838.
- [172] T. Majumder, S. Dhar, K. Debnath, S. P. Mondal, *Mater. Res. Bull.* **2017**, 93, 214.
- [173] Z. Liu, Y. Wang, B. Wang, Y. Li, Z. Liu, J. Han, K. Guo, Y. Li, T. Cui, L. Han, C. Liu, G. Li, *Int. J. Hydrogen Energy* **2013**, 38, 10226.
- [174] K. Shin, S. i. Seok, S. H. Im, J. H. Park, *Chem. Commun.* **2010**, 46, 2385.
- [175] D. Wang, T. Sheng, J. Chen, H.-F. Wang, P. Hu, *Nat. Catal.* **2018**, 1, 291.
- [176] G. Xie, L. Guan, L. Zhang, B. Guo, A. Batool, Q. Xin, R. Boddula, S. U. Jan, J. R. Gong, *Nano Lett.* **2019**, 19, 1234.
- [177] S. Bai, J. Jiang, Q. Zhang, Y. Xiong, *Chem. Soc. Rev.* **2015**, 44, 2893.
- [178] R. Lv, T. Wang, F. Su, P. Zhang, C. Li, J. Gong, *Nano Energy* **2014**, 7, 143.
- [179] I. S. Cho, Z. Chen, A. J. Forman, D. R. Kim, P. M. Rao, T. F. Jaramillo, X. Zheng, *Nano Lett.* **2011**, 11, 4978.
- [180] R. Zhang, L. Yang, X. Huang, T. Chen, F. Qu, Z. Liu, G. Du, A. M. Asiri, X. Sun, *J. Mater. Chem. A* **2017**, 5, 12086.
- [181] S. Kim, M. A. Mahadik, W.-S. Chae, J. Ryu, S. H. Choi, J. S. Jang, *Appl. Surf. Sci.* **2020**, 513, 145528.
- [182] Z. Tian, X. Guo, D. Wang, D. Sun, S. Zhang, K. Bu, W. Zhao, F. Huang, *Adv. Funct. Mater.* **2020**, 30, 2001286.
- [183] G. Wang, H. Wang, Y. Ling, Y. Tang, X. Yang, R. C. Fitzmorris, C. Wang, J. Z. Zhang, Y. Li, *Nano Lett.* **2011**, 11, 3026.
- [184] M. Xu, P. Da, H. Wu, D. Zhao, G. Zheng, *Nano Lett.* **2012**, 12, 1503.
- [185] S. Shen, J. Jiang, P. Guo, C. X. Kronawitter, S. S. Mao, L. Guo, *Nano Energy* **2012**, 1, 732.
- [186] H. Zheng, Y. Li, H. Liu, X. Yin, Y. Li, *Chem. Soc. Rev.* **2011**, 40, 4506.
- [187] N. Chen, Y. Hu, X. Liu, J. Yang, W. Li, D. Lu, J. Fu, Y. Liang, W. Wang, *J. Phys. Chem. C* **2020**, 124, 21968.
- [188] S. Sadhasivam, N. Anbarasan, M. Mukilan, P. Manivel, K. Jeganathan, *Int. J. Hydrogen Energy* **2020**, 45, 30080.
- [189] X. Zou, H. Fan, Y. Tian, S. Yan, *CrystEngComm* **2014**, 16, 1149.
- [190] N. Wang, M. Liu, H. Tan, J. Liang, Q. Zhang, C. Wei, Y. Zhao, E. H. Sargent, X. Zhang, *Small* **2017**, 13, 1603527.
- [191] H. Wang, L. Zhang, Z. Chen, J. Hu, S. Li, Z. Wang, J. Liu, X. Wang, *Chem. Soc. Rev.* **2014**, 43, 5234.
- [192] Y. Wang, Q. Wang, X. Zhan, F. Wang, M. Safdar, J. He, *Nanoscale* **2013**, 5, 8326.
- [193] J. Hou, C. Yang, H. Cheng, S. Jiao, O. Takeda, H. Zhu, *Energy Environ. Sci.* **2014**, 7, 3758.
- [194] H. Li, Y. Gao, Y. Zhou, F. Fan, Q. Han, Q. Xu, X. Wang, M. Xiao, C. Li, Z. Zou, *Nano Lett.* **2016**, 16, 5547.
- [195] F. Wu, Y. Yu, H. Yang, L. N. German, Z. Li, J. Chen, W. Yang, L. Huang, W. Shi, L. Wang, X. Wang, *Adv. Mater.* **2017**, 29, 1701432.
- [196] Y. Chen, H. Jiang, L. Li, Q. Wang, L. Du, X. Liu, G. Tian, *Int. J. Hydrogen Energy* **2020**, 45, 6174.

- [197] Y. Wang, Y. Liang, D. Zeng, M. Zhu, J. Fu, T. Zhu, H. Han, C. Li, W. Wang, *Electrochim. Acta* **2020**, 337, 135763.
- [198] H. Li, B. Liu, S. Feng, H. Li, T. Wang, J. Gong, *J. Mater. Chem. A* **2020**, 8, 224.
- [199] G. Dai, J. Yu, G. Liu, *J. Phys. Chem. C* **2011**, 115, 7339.
- [200] H. Jiang, Y. Chen, L. Li, H. Liu, C. Ren, X. Liu, G. Tian, *J. Alloys Compd.* **2020**, 828, 154449.
- [201] L. Yao, W. Wang, T. Zhu, Y. Wang, Y. Liang, J. Fu, J. Wang, Y. Cheng, S. Liu, *Appl. Catal., B* **2020**, 268, 118460.
- [202] B. R. Lee, M. G. Lee, H. Park, T. H. Lee, S. A. Lee, S. S. M. Bhat, C. Kim, S. Lee, H. W. Jang, *ACS Appl. Mater. Interfaces* **2019**, 11, 20004.
- [203] G. Ghadimkhani, N. R. de Tacconi, W. Chanmanee, C. Janaky, K. Rajeshwar, *Chem. Commun.* **2013**, 49, 1297.
- [204] P. Zhou, J. Yu, M. Jaroniec, *Adv. Mater.* **2014**, 26, 4920.
- [205] H. Li, W. Tu, Y. Zhou, Z. Zou, *Adv. Sci.* **2016**, 3, 1500389.
- [206] P. Li, Y. Zhou, H. Li, Q. Xu, X. Meng, X. Wang, M. Xiao, Z. Zou, *Chem. Commun.* **2015**, 51, 800.
- [207] C. Kim, K. M. Cho, A. Al-Saggaf, I. Gereige, H.-T. Jung, *ACS Catal.* **2018**, 8, 4170.
- [208] T. Zhou, J. Wang, S. Chen, J. Bai, J. Li, Y. Zhang, L. Li, L. Xia, M. Rahim, Q. Xu, B. Zhou, *Appl. Catal., B* **2020**, 267, 118599.
- [209] G. Zheng, J. Wang, H. Li, Y. Li, P. Hu, *Appl. Catal., B* **2020**, 265, 118561.
- [210] L. Zhang, H. Cao, Y. Lu, H. Zhang, G. Hou, Y. Tang, G. Zheng, *J. Colloid Interface Sci.* **2020**, 568, 198.
- [211] A. Zhu, Q. Zhao, X. Li, Y. Shi, *ACS Appl. Mater. Interfaces* **2014**, 6, 671.
- [212] F. Su, T. Wang, R. Lv, J. Zhang, P. Zhang, J. Lu, J. Gong, *Nanoscale* **2013**, 5, 9001.
- [213] J. Yang, C. Bao, T. Yu, Y. Hu, W. Luo, W. Zhu, G. Fu, Z. Li, H. Gao, F. Li, Z. Zou, *ACS Appl. Mater. Interfaces* **2015**, 7, 26482.
- [214] J. Hou, H. Cheng, O. Takeda, H. Zhu, *Angew. Chem., Int. Ed.* **2015**, 54, 8480.
- [215] J. He, M. Wang, X. Wu, Y. Sun, K. Huang, H. Chen, L. Gao, S. Feng, *J. Alloys Compd.* **2019**, 785, 391.
- [216] W. Fan, S. Jewell, Y. She, M. K. H. Leung, *Phys. Chem. Chem. Phys.* **2014**, 16, 676.
- [217] Y.-F. Xu, H.-S. Rao, X.-D. Wang, H.-Y. Chen, D.-B. Kuang, C.-Y. Su, *J. Mater. Chem. A* **2016**, 4, 5124.
- [218] Y. Lin, S. Zhou, X. Liu, S. Sheehan, D. Wang, *J. Am. Chem. Soc.* **2009**, 131, 2772.
- [219] W. Wang, B. Guo, H. Dai, C. Zhao, G. Xie, R. Ma, M. Z. Akram, H. Shan, C. Cai, Z. Fang, J. R. Gong, *Nano Lett.* **2019**, 19, 6133.
- [220] K. Tvingstedt, N.-K. Persson, O. Inganäs, A. Rahachou, I. V. Zozoulenko, *Appl. Phys. Lett.* **2007**, 91, 113514.
- [221] P. Spinelli, M. Hebbink, R. de Waele, L. Black, F. Lenzmann, A. Polman, *Nano Lett.* **2011**, 11, 1760.
- [222] H. A. Atwater, A. Polman, *Nat. Mater.* **2010**, 9, 205.
- [223] J. Zhang, M. Zhang, R.-Q. Sun, X. Wang, *Angew. Chem., Int. Ed.* **2012**, 51, 10145.
- [224] J. S. Jang, H. G. Kim, J. S. Lee, *Catal. Today* **2012**, 185, 270.
- [225] H. G. Kim, P. H. Borse, W. Choi, J. S. Lee, *Angew. Chem., Int. Ed.* **2005**, 44, 4585.
- [226] H. Huang, K. Xiao, X. Du, Y. Zhang, *ACS Sustainable Chem. Eng.* **2017**, 5, 5253.
- [227] K. Zhang, Y. Dai, Z. Zhou, S. Ullah Jan, L. Guo, J. R. Gong, *Nano Energy* **2017**, 41, 101.
- [228] L. Li, L. Jin, J. Wang, D. J. Smith, W.-J. Yin, Y. Yan, H. Sang, W. C. H. Choy, M. R. McCartney, *Adv. Mater.* **2012**, 24, 1328.
- [229] B. Mei, B. Seger, T. Pedersen, M. Malizia, O. Hansen, I. Chorkendorff, P. C. K. Vesborg, *J. Phys. Chem. Lett.* **2014**, 5, 1948.
- [230] M. J. Kenney, M. Gong, Y. Li, J. Z. Wu, J. Feng, M. Lanza, H. Dai, *Science* **2013**, 342, 836.
- [231] X. Yu, P. Yang, S. Chen, M. Zhang, G. Shi, *Adv. Energy Mater.* **2017**, 7, 1601805.
- [232] T. W. Kim, K.-S. Choi, *Science* **2014**, 343, 990.
- [233] B. Guo, A. Batool, G. Xie, R. Boddula, L. Tian, S. U. Jan, J. R. Gong, *Nano Lett.* **2018**, 18, 1516.
- [234] D. Li, J. Shi, C. Li, *Small* **2018**, 14, 1704179.
- [235] L.-L. Feng, G. Yu, Y. Wu, G.-D. Li, H. Li, Y. Sun, T. Asefa, W. Chen, X. Zou, *J. Am. Chem. Soc.* **2015**, 137, 14023.
- [236] M. Z. Akram, V. Atla, A. Nambo, B. P. Ajayi, J. B. Jasinski, J. He, J. R. Gong, M. Sunkara, *Nano Lett.* **2018**, 18, 4891.
- [237] Z. Luo, T. Wang, J. Gong, *Chem. Soc. Rev.* **2019**, 48, 2158.
- [238] L. Ji, M. D. McDaniel, S. Wang, A. B. Posadas, X. Li, H. Huang, J. C. Lee, A. A. Demkov, A. J. Bard, J. G. Ekerdt, E. T. Yu, *Nat. Nanotechnol.* **2014**, 10, 84.
- [239] J. T. Song, H. Ryoo, M. Cho, J. Kim, J.-G. Kim, S.-Y. Chung, J. Oh, *Adv. Energy Mater.* **2017**, 7, 1601103.
- [240] S. Oh, H. Song, J. Oh, *Nano Lett.* **2017**, 17, 5416.
- [241] S. Oh, J. Oh, *J. Phys. Chem. C* **2016**, 120, 133.
- [242] K. Sun, N. L. Ritzert, J. John, H. Tan, W. G. Hale, J. Jiang, I. Moreno-Hernandez, K. M. Papadantonakis, T. P. Moffat, B. S. Brunschwig, N. S. Lewis, *Sustainable Energy Fuels* **2018**, 2, 983.
- [243] Y. Chen, K. Sun, H. Audesirk, C. Xiang, N. S. Lewis, *Energy Environ. Sci.* **2015**, 8, 1736.
- [244] M. R. Shaner, J. R. McKone, H. B. Gray, N. S. Lewis, *Energy Environ. Sci.* **2015**, 8, 2977.
- [245] W. Vijsselaar, P. Westerik, J. Veerbeek, R. M. Tiggelaar, E. Berenschat, N. R. Tas, H. Gardeniers, J. Huskens, *Nat. Energy* **2018**, 3, 185.
- [246] H. Lin, X. Long, Y. An, D. Zhou, S. Yang, *Nano Lett.* **2019**, 19, 455.
- [247] S. Hoang, S. Guo, N. T. Hahn, A. J. Bard, C. B. Mullins, *Nano Lett.* **2012**, 12, 26.
- [248] M. Ye, J. Gong, Y. Lai, C. Lin, Z. Lin, *J. Am. Chem. Soc.* **2012**, 134, 15720.
- [249] Y. Mao, H. Yang, J. Chen, J. Chen, Y. Tong, X. Wang, *Nano Energy* **2014**, 6, 10.
- [250] X. Fan, B. Gao, T. Wang, X. Huang, H. Gong, H. Xue, H. Guo, L. Song, W. Xia, J. He, *Appl. Catal., A* **2016**, 528, 52.
- [251] L. Wei, J. Lin, S. Xie, W. Ma, Q. Zhang, Z. Shen, Y. Wang, *Nanoscale* **2019**, 11, 12530.
- [252] B. AlOtaibi, S. Fan, D. Wang, J. Ye, Z. Mi, *ACS Catal.* **2015**, 5, 5342.
- [253] S. Chu, P. Ou, P. Ghamari, S. Vanka, B. Zhou, I. Shih, J. Song, Z. Mi, *J. Am. Chem. Soc.* **2018**, 140, 7869.
- [254] B. Shan, S. Vanka, T.-T. Li, L. Troian-Gautier, M. K. Brenneman, Z. Mi, T. J. Meyer, *Nat. Energy* **2019**, 4, 290.
- [255] X. Chang, T. Wang, P. Yang, G. Zhang, J. Gong, *Adv. Mater.* **2019**, 31, 1804710.
- [256] Y. Y. Birdja, E. Pérez-Gallent, M. C. Figueiredo, A. J. Göttle, F. Calle-Vallejo, M. T. M. Koper, *Nat. Energy* **2019**, 4, 732.
- [257] W. Zhu, Y.-J. Zhang, H. Zhang, H. Lv, Q. Li, R. Michalsky, A. A. Peterson, S. Sun, *J. Am. Chem. Soc.* **2014**, 136, 16132.
- [258] Q. Shen, Z. Chen, X. Huang, M. Liu, G. Zhao, *Environ. Sci. Technol.* **2015**, 49, 5828.
- [259] Q. Shen, X. Huang, J. Liu, C. Guo, G. Zhao, *Appl. Catal., B* **2017**, 201, 70.
- [260] J. Li, X. Feng, J. Fei, P. Cai, J. Huang, J. Li, *J. Mater. Chem. A* **2016**, 4, 12197.
- [261] D. Mersch, C.-Y. Lee, J. Z. Zhang, K. Brinkert, J. C. Fontecilla-Camps, A. W. Rutherford, E. Reisner, *J. Am. Chem. Soc.* **2015**, 137, 8541.
- [262] J. Ryu, S. H. Lee, D. H. Nam, C. B. Park, *Adv. Mater.* **2011**, 23, 1883.
- [263] J. Liu, R. Cazelles, Z. P. Chen, H. Zhou, A. Galarneau, M. Antonietti, *Phys. Chem. Chem. Phys.* **2014**, 16, 14699.
- [264] S. H. Lee, G. M. Ryu, D. H. Nam, J. H. Kim, C. B. Park, *ChemSusChem* **2014**, 7, 3007.

- [265] C. Liu, J. J. Gallagher, K. K. Sakimoto, E. M. Nichols, C. J. Chang, M. C. Y. Chang, P. Yang, *Nano Lett.* **2015**, *15*, 3634.
- [266] R. E. Blankenship, D. M. Tiede, J. Barber, G. W. Brudvig, G. Fleming, M. Ghirardi, M. R. Gunner, W. Junge, D. M. Kramer, A. Melis, T. A. Moore, C. C. Moser, D. G. Nocera, A. J. Nozik, D. R. Ort, W. W. Parson, R. C. Prince, R. T. Sayre, *Science* **2011**, *332*, 805.
- [267] N. Kornienko, J. Z. Zhang, K. K. Sakimoto, P. Yang, E. Reisner, *Nat. Nanotechnol.* **2018**, *13*, 890.
- [268] J. A. Maciá-Agulló, A. Corma, H. Garcia, *Chem. - Eur. J.* **2015**, *21*, 10940.
- [269] S. H. Lee, D. S. Choi, S. K. Kuk, C. B. Park, *Angew. Chem., Int. Ed.* **2018**, *57*, 7958.
- [270] E. Reisner, D. J. Powell, C. Cavazza, J. C. Fontecilla-Camps, F. A. Armstrong, *J. Am. Chem. Soc.* **2009**, *131*, 18457.
- [271] B. Chica, C.-H. Wu, Y. Liu, M. W. W. Adams, T. Lian, R. B. Dyer, *Energy Environ. Sci.* **2017**, *10*, 2245.
- [272] K. A. Brown, D. F. Harris, M. B. Wilker, A. Rasmussen, N. Khadka, H. Hamby, S. Keable, G. Dukovic, J. W. Peters, L. C. Seefeldt, P. W. King, *Science* **2016**, *352*, 448.
- [273] W. Wang, Z. Wang, Q. Zhu, G. Han, C. Ding, J. Chen, J.-R. Shen, C. Li, *Chem. Commun.* **2015**, *51*, 16952.
- [274] K. P. Sokol, W. E. Robinson, J. Warnan, N. Kornienko, M. M. Nowaczyk, A. Ruff, J. Z. Zhang, E. Reisner, *Nat. Energy* **2018**, *3*, 944.
- [275] S. K. Kuk, R. K. Singh, D. H. Nam, R. Singh, J.-K. Lee, C. B. Park, *Angew. Chem., Int. Ed.* **2017**, *56*, 3827.
- [276] C. C. C. R. de Carvalho, *Biotechnol. Adv.* **2011**, *29*, 75.
- [277] D. R. MacFarlane, J. Choi, B. H. R. Suryanto, R. Jalili, M. Chatti, L. M. Azofra, A. N. Simonov, *Adv. Mater.* **2020**, *32*, 1904804.
- [278] G. Liu, N. Hoivik, K. Wang, H. Jakobsen, *Sol. Energy Mater. Sol. Cells* **2012**, *105*, 53.
- [279] J. Li, Y. Tian, Y. Zhou, Y. Zong, N. Yang, M. Zhang, Z. Guo, H. Song, *Trans. Tianjin Univ.* **2020**, *26*, 237.



**Liangqiu Tian** received her B.S. degree in nanomaterials and technology from Beijing Jiaotong University and the University of Waterloo in 2017, and received her M.S. degree in physical chemistry from the University of Chinese Academy of Sciences (CAS), China, in 2021. Her research interests focus on the carbon nitride-based photocatalysts and exciton dynamics for hydrogen evolution.



**Qi Xin** graduated from Zhou Kou Normal University in 2007, and completed his Ph.D. program in plant science from China Agricultural University in 2013. After that, he joined the National Center for Nanoscience and Technology (NCNST). His research interests focus on the carbon-based nanomaterials and their biomedical and photocatalytic applications.



**Chang Zhao** received her B.S. degree in new energy materials from devices from Xiangtan University in 2016 and her M.S. degree in physical chemistry from the University of CAS in 2019. Her research interest focuses on the Si-based photoanode for photoelectrochemical water splitting.



**Guancai Xie** received his Ph.D. in condensed matter physics from the University of CAS, China, in 2020. He is now a postdoctoral fellow in NCNST, China. His research interests focus on the design and understanding of 2D nanomaterial-based photocatalysts and photoelectrodes for solar water splitting.



**Muhammad Zain Akram** earned his Ph.D. in material science and engineering from the University of CAS in 2019. He later joined the chemical vapor deposition (CVD) lab at Conn Center of Renewable Energy Research, University of Louisville, USA, as a postdoctoral researcher. Dr. Akram has expertise in CVD techniques for the growth of nanomaterials. His research focuses on scalable synthesis and applications of nanomaterial for energy conversion and storage, carbon capture, wastewater treatment, and single-crystal diamond growth using microwave plasma CVD.



**Wenrong Wang** received her B.S. degree in applied physics from Chongqing University in 2012. She is a Ph.D. student at Chongqing University. Now she is a jointly educates student at NCNST. Her research interests focus on the hematite-based nanomaterial for photoelectrochemical water splitting.



**Renping Ma** received her B.S. degree in chemistry from Jilin University in 2009 and received her Ph.D. degree in physical chemistry from Jilin University in 2014. Now she is a postdoctoral fellow at NCNST. Her research interests focus on regularly patterned electrodes for photoelectrochemical water splitting.



**Xinrui Jia** is currently a Ph.D. candidate in NCNST. Her research focuses on the photoelectrocatalysis.



**Beidou Guo** received his Ph.D. degree from the University of CAS, China, in 2021. He is now an assistant professor in condensed matter physics at the NCNST, China. His research focuses on renewable energy, electronic materials, and devices.



**Jian Ru Gong** is a professor at NCNST, China. Her current research interest focuses on design and preparation of novel nanoscale materials and devices, and their applications for green renewable energy. For more details, please visit the Gong group website: <http://www.nanoctr.cn/gongjianru>